

Article

Integrated Earthquake Catalog III: Gakkel Ridge, Knipovich Ridge, and Svalbard Archipelago

Inessa A. Vorobieva^{1,2}, Alexei D. Gvishiani^{1,3}, Peter N. Shebalin^{1,2} , Boris A. Dzeboev^{1,*} ,
Boris V. Dzeranov¹ , Natalia A. Sergeeva¹, Ernest O. Kedrov¹  and Yuliya V. Barykina¹

¹ Geophysical Center of the Russian Academy of Sciences (GC RAS), 119296 Moscow, Russia; vorobiev@mitp.ru (I.A.V.); a.gvishiani@gcras.ru (A.D.G.); p.n.shebalin@gmail.com (P.N.S.); b.dzeranov@gcras.ru (B.V.D.); n.sergeyeva@gcras.ru (N.A.S.); e.kedrov@gcras.ru (E.O.K.); u.barykina@gcras.ru (Y.V.B.)

² Institute of Earthquake Prediction Theory and Mathematical Geophysics of the Russian Academy of Sciences (IEPT RAS), 117997 Moscow, Russia

³ Schmidt Institute of Physics of the Earth of the Russian Academy of Sciences (IPE RAS), 119296 Moscow, Russia

* Correspondence: b.dzeboev@gcras.ru; Tel.: +7-495-930-05-46

Abstract: This paper represents the final part of a series of studies aimed at creating the most reliable and representative earthquake catalog covering the Russian and European Arctic. The earthquake catalog of the Gakkel and Knipovich ridges, as well as the Svalbard Archipelago with a unified magnitude scale, was formed based on the combination of four regional Russian catalogs and the ISC catalog. The merging of catalogs was carried out using the modification of the author's methodology, which allowed for the identification of records in different datasets related to the same seismic event. The modification was introduced due to significant changes over time in the source catalogs. The unified proxy moment magnitude scale was formed based on regression analysis of the different magnitude estimates provided by various agencies. The integrated catalog included 17,922 earthquakes that occurred during the period 1962–2022. Analysis of the integrated catalog showed that the level of registration in the studied area significantly varies over space and time. Before 1995, the catalog contained only strong and moderate earthquakes, and the magnitude of complete registration M_c was 5.0 in the Gakkel Ridge, 4.7 in the Knipovich Ridge, and 4.5 in the Svalbard Archipelago. The number of recorded events increased in the period 1995–2011, and M_c decreased to 4.0 in the Gakkel and Knipovich ridges and to 2.8 in the Svalbard Archipelago. The best level of registration in the Svalbard Archipelago and the Knipovich Ridge was achieved after 2012, when M_c reached 1.7 and 2.8, respectively. In the Gakkel Ridge, despite a noticeable increase in the number of reported events from 2012, the magnitude of complete registration did not improve and was 4.0. The presented integrated earthquake catalog is intended for a wide range of studies of the seismic regime of the Arctic.



Citation: Vorobieva, I.A.; Gvishiani, A.D.; Shebalin, P.N.; Dzeboev, B.A.; Dzeranov, B.V.; Sergeeva, N.A.; Kedrov, E.O.; Barykina, Y.V. Integrated Earthquake Catalog III: Gakkel Ridge, Knipovich Ridge, and Svalbard Archipelago. *Appl. Sci.* **2023**, *13*, 12422. <https://doi.org/10.3390/app132212422>

Academic Editor: Fabrizio Balsamo

Received: 22 September 2023

Revised: 7 November 2023

Accepted: 13 November 2023

Published: 16 November 2023

Keywords: Arctic; Gakkel Ridge; Knipovich Ridge; Svalbard Archipelago; merging earthquake catalogs; magnitude unification; level of registration



Copyright: © 2023 by the authors. Licensee MDPI, Basel, Switzerland. This article is an open access article distributed under the terms and conditions of the Creative Commons Attribution (CC BY) license (<https://creativecommons.org/licenses/by/4.0/>).

1. Introduction

The seismicity of the territory occupied by the Svalbard Archipelago and the Gakkel and Knipovich ridges within the Arctic Ocean is studied in the present paper. These ridges are a part of the Mid-Ocean Ridges (MOR) system. The Gakkel Ridge forms the divergent boundary between the North American and Eurasian lithosphere plates in the Arctic Ocean. It extends in a sub-parallel direction for 1800 km from the Laptev Sea continental margin, transitioning to the west through a complex combination of transform faults and rifts (Spitsbergen and Molloy fracture zones) into the Knipovich Ridge, the northernmost fragment of the Mid-Atlantic Ridge (Figure 1).

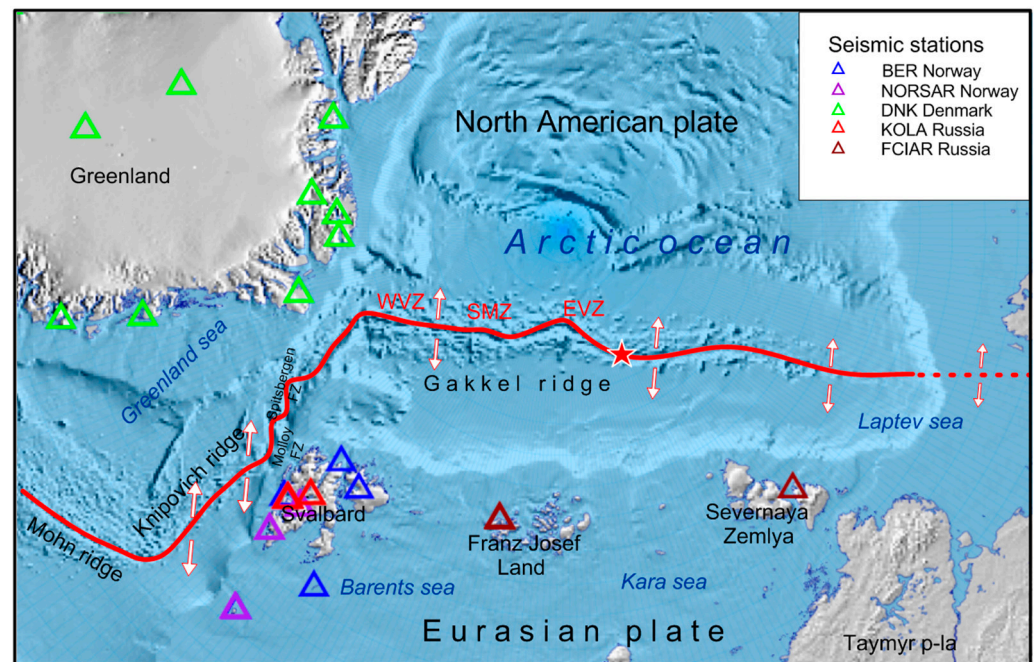


Figure 1. Scheme of the Arctic region and seismic networks. The red line is the boundary between North American and Eurasian plates. The red dotted line is the part of the boundary after the Gakkel ridge. WVZ and EVZ are the Eastern and the Western Volcanic Zones in the Gakkel ridge, and SMZ is the Sparsely Magmatic Zone [1,2]; a star marks the location of volcanic eruption and earthquake swarm in 1999 [3,4]. Arrows show the spreading direction. Triangles are seismic stations of European and Russian networks (see legend).

The Gakkel Ridge is the center of spreading for the Eurasian basin and belongs to the ultra-slow spreading rift zones. It is characterized by the lowest spreading rates among the entire MOR system. The maximum spreading rate in the orthogonal direction ranges from 6–7 mm/year in the east to 9–13 mm/year in the west [5,6]. The distance between volcanic areas along the Gakkel Ridge is 110–130 km. They are located perpendicularly to the ridge axis. It should be noted that the Gakkel Ridge is undisturbed by transform faults [7–9]. Similar characteristics of spreading rates and structure are also present in the eastern segment of the Southwest Indian Ridge. This is reflected in similar seismic activity features that distinguish these ridges from ridges with slow and medium spreading rates [10].

Based on the morphological features and deep structure, the Gakkel Ridge is divided into three provinces: the Western Volcanic Zone (WVZ) (7° W– 3° E), the central Sparsely Magmatic Zone (SMZ) (3° E– 30° E), and the Eastern Volcanic Zone (EVZ) (30° E– 85° E) [1,2]. Despite its lower spreading rate, the WVZ is characterized by extensive magmatic processes, which are reflected in the similarity of its relief to that of the Mid-Atlantic Ridge rift zone. The maximum depth of the WVZ reaches 4.3 km. The length of volcanic ridges identified in its central part ranges from 15 to 50 km, with heights ranging from 0.4 to 1.4 km. The rift valley is composed of basalts, and several hydrothermal plumes have been identified within it [7,11,12]. In contrast, the SMZ is characterized by rare manifestations of magmatism, with a single large volcanic center located in the 19° E area. The maximum depth of the rift valley is 4.8–5.4 km [6,7,12].

Within the EVZ, extended amagmatic sections with gentle slopes and lengths of 40–120 km separated by volcanic centers can be distinguished. The maximum depth of the amagmatic sections is 4.8–5.1 km. The largest volcanic center of the Gakkel Ridge is located in the eastern part of the segment, in the 85° E area [6,7,12]. In 1999, an unprecedented surge in seismic activity was recorded there. It was caused by an effusive-explosive underwater volcanic eruption. The seismic network deployed on ice floes allowed for the registration of a swarm of 209 events with hypocenter depths up to 25 km [3,4]. Based on the data

obtained in [13], a seismic tomography model was constructed. The combination of ultra-slow spreading rates with low potential mantle temperatures leads to the production of low-temperature, volatile-rich magmatic melts. Explosive underwater eruptions occur as a result of the degassing of these melts [13,14].

Maximum magnitudes are recorded in the eastern segment of the Gakkel Ridge (in the Laptev Sea). The strongest earthquake within the Gakkel Ridge, with $M_S = 6.5$ (International Seismological Centre), occurred there on 25 August 1964 [15]. The epicenters of two earthquakes with $M_W = 6.4$ and $M_W = 6.2$ (Global Centroid-Moment-Tensor), which occurred on 21 March 1988 and 6 March 2005, respectively, were also located in this area [16].

The Svalbard Archipelago includes more than a thousand small and large islands, among which West Spitsbergen, Prince Charles Land, Barents Island, Edge, and Northeast Land can be distinguished. More than half of the archipelago's area is covered by glaciers. The first temporary seismic station was installed in Longyearbyen. Subsequently, several analog stations were installed in Kapp Linné (1958–1963), Ny-Ålesund (1967), Hornsund (1978), Barentsburg (1979), and Pyramididen (1982–1989). In addition, several large-scale seismic surveys were conducted on Phipps Island, Southern Spitsbergen, and Northeast Land in 1976–1986 to study the tectonic structure of the region [17,18].

It should be noted that, until the 1970s, numerous researchers believed that the most seismically active zone in the Svalbard region was the area of the Mohn and Knipovich ridges. The territory of the archipelago itself was considered to be seismically quiet. However, on 18 January 1976, an earthquake with $M = 5.7$ occurred on the eastern coast of West Spitsbergen in the Storfjorden, which caused a revision of these views. On 21 February 2008, the strongest earthquake for the archipelago, with $M_w = 6.1$, was recorded in the same area [18,19].

Over the past few decades, the seismic network of the Svalbard Archipelago has continuously expanded and developed. Today, it consists of stationary stations equipped with digital seismometers and serves as a backbone network for cryoseismological research in the region. The seismic stations of NORSAR, GSN, GEOFON, and IGF PAS operate on the territory of the archipelago. In 2010, two seismic stations were installed in Barentsburg by the Kola Science Centre of the Russian Academy of Sciences, in collaboration with NORSAR [17,18].

The Knipovich Ridge stretches for 550 km along the continental margin of the Svalbard Archipelago from $73^{\circ}45'$ to $78^{\circ}35'$ N. It is a section of mid-ocean ridges with an ultra-slow spreading rate of 15–17 mm/year. Like the Gakkel Ridge, it is not disrupted by transform faults [20,21]. Within the rift valley, magmatic and amagmatic segments can be distinguished. Magmatic segments are represented by volcanic ridges oriented perpendicularly to the direction of extension. Amagmatic segments are expressed as deep depressions on the rift valley floor located parallel to its axis [9].

Earthquakes with magnitudes of $M_W^{ISCGEM} = 6.54$ and $M_W^{GCMT} = 6.1$ that occurred on 1 June 1915 and 9 September 1992, respectively, were the strongest events in the area of the Knipovich Ridge [15,16]. The epicenters of three earthquakes with magnitudes of $M_W^{GCMT} = 5.4$, which occurred on 3 February 2000, 21 June 2009, and 22 June 2009, were also confined to the Knipovich Ridge [16].

At the same time, the strongest earthquake in the considered region was an event with a magnitude of $M_W^{GCMT} = 6.7$, which occurred on 20.07.1992 in the Molloy transform fault. Also, the epicenters of four earthquakes with a magnitude of $M_W^{GCMT} \geq 6.0$ were confined to the Molloy transform fault and Spitsbergen fracture zones area [16].

Until recently, earthquakes on the Gakkel and Knipovich ridges were only recorded at teleseismic distances with thresholds ranging from $M \geq 4.5$ to $M \geq 3.5$ for different segments. Information on weak seismicity is valuable for studying tectonic and volcanic processes occurring in rift zones. In this regard, it should be noted that the installation of stationary seismic stations of the Arkhangelsk seismic network on the Arctic archipelagos of Franz Josef Land and Severnaya Zemlya in 2012 allowed for the registering of low-magnitude events within the Gakkel Ridge at closer distances [22,23]. It should be also

noted that stations located in Svalbard (BERGEN, NORSAR, and KOLA) and Greenland (DNK) contribute to the registration of low-magnitude events within the Knipovich Ridge.

The earthquake catalog of the Gakkel and Knipovich ridges is a fundamental basis for studying seismicity, regional segmentation, and seismotectonics of the poorly studied boundary between the Eurasian and North American plates. It should be noted that, in [24], the earthquake catalog was created, covering the area north of 72° N for the period 1955–1999. Using regional bathymetry and potential fields, a seismicity model was obtained and a segmentation of the interplate boundary was proposed.

The present paper aims to create a unified integrated earthquake catalog of the Gakkel and Knipovich ridges, as well as the Svalbard Archipelago, merging all available data from Russian and international agencies. The author's methodology of intelligent merging (with the identification of formed duplicate events and their separation from aftershocks [25]) of earthquake catalogs from different networks and seismological agencies is described in detail in [26]. The unified integrated earthquake catalogs that were created using this methodology for the eastern and western sectors of the Russian Arctic zone are available to the public at: http://www.wdcb.ru/arctic_antarctic/arctic_seism.html (accessed on 1 August 2023), and a description of the assembly process is given in [27,28].

Therefore, this article, along with the results by the authors in [26–28], completes the creation of the most reliable integrated unified earthquake catalogs that cover the whole Russian and European Arctic.

2. Materials and Methods

The region considered in the present paper (Figure 2) covers zones that were not included in the Eastern (catalog I) and Western (catalog II) sectors of the Russian Arctic. The territory is directly adjacent to the Eastern and Western sectors, but does not intersect with them. The schematic coverage map for catalogs I, II, and III is presented in (Figure S1, see Supplementary).

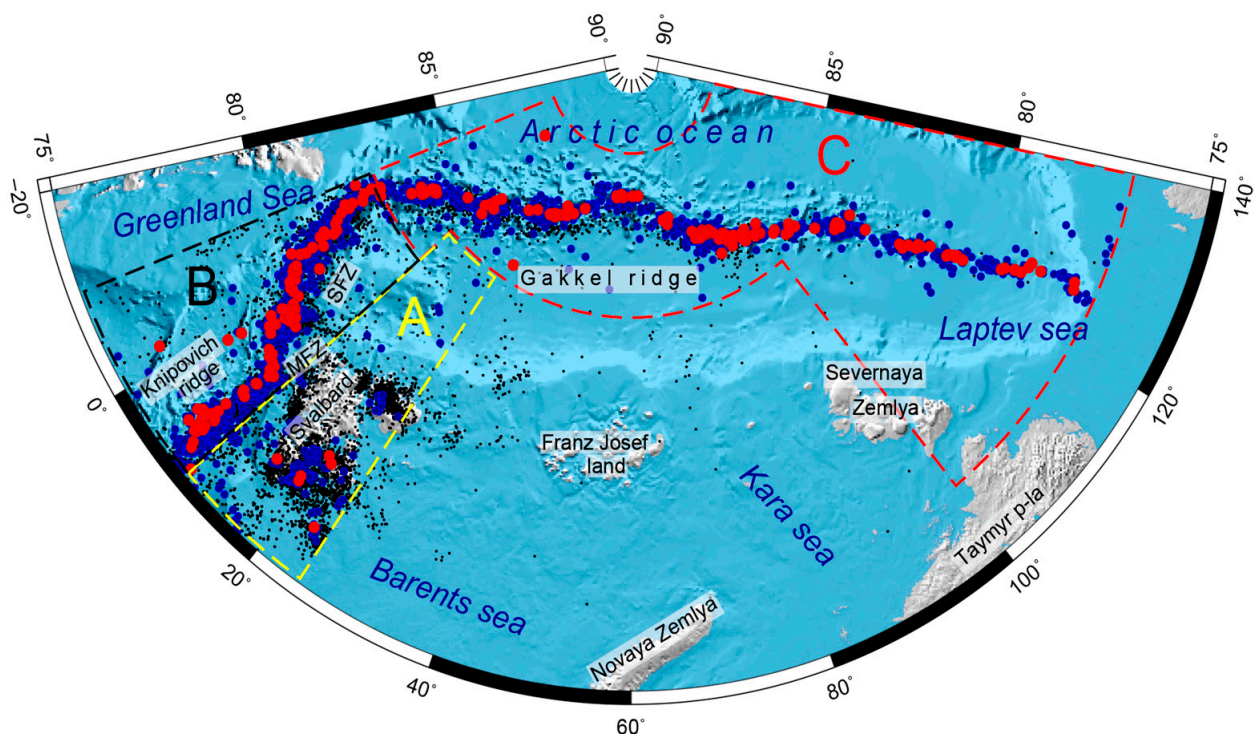


Figure 2. Map of the studied region with earthquake epicenters from the ISC catalog: events with mb^{ISC} and mb^{NEIC} magnitude determinations are marked in blue, and events with Mw^{GCMT} determinations are marked in red. MFZ and SFZ are Molloy and Spitsbergen fracture zones. Dashed lines delineate sub-regions Svalbard (A), Knipovich (B), and Gakkel (C).

The set of initial data was compiled from five earthquake catalogs (Table 1):

1. The Arctic catalog from the annual journals Earthquakes in the USSR 1962–1991, Earthquakes in Northern Eurasia 1992–2017, and Earthquakes in Russia 2018–2021 (hereinafter ARC);
2. The catalog of the FCIAR network (Arkhangelsk network) 2008–2017 from the annual journals of Earthquakes in Northern Eurasia (hereinafter ARKH);
3. The catalog of the Svalbard Archipelago territory for 2010–2021 from the annual journals of Earthquakes in Russia (hereinafter SHB);
4. The ISC 1962–2022 catalog, which is a composite and contains data from many world and also Russian agencies (Table S1, see Supplementary);
5. The catalog Seismicity of the western sector of the Russian Arctic for 1962–2020 [29] (hereinafter Morozov). The Morozov catalog was recently presented in [29]. In this catalog, earthquakes are relocated based on the analysis and merging of all available seismic bulletins from Russian and European seismic networks using modern velocity models. The Morozov catalog covers the shelf zone of the Western Sector of the Russian Arctic, which we included in our previous study [28], but some earthquakes were relocated [29] from the shelf to the Gakkel Ridge. We include these events in our catalog, since we consider determinations [29] to be the most reliable.

According to [30,31], a large number of small seismic events registered in the Svalbard archipelago are ice-quakes. Such events are not presented in Russian catalogs. The ISC catalog includes 16 non-earthquake events (explosions and glacial events), all of them in Svalbard. One of these events is presented in the ARC catalog and another in the ARKH catalog. These events were excluded from the source catalogs. No additional checks were performed after merging the catalogs.

According to [30,31], a large number of seismic events registered in the Svalbard Archipelago with magnitudes ranging from 1 to 2.2 are ice-quakes. This is confirmed, among other things, by a seasonal periodicity that is not typical for earthquakes. However, in the ISC catalog, only 6 events were marked as glacial events (ice-quakes). Either the ice-quakes were cleared out by the compilers, or most of the events were still earthquakes. More than 90% of the events had a significant depth, which is not typical for ice-quakes, so we considered them earthquakes and included them in the integrated catalog (Figure S1, see Supplementary).

Events with unknown magnitude/class were excluded from consideration. Earthquakes were selected within the boundaries of the studied region (Figure S2, see Supplementary).

Table 1. Input catalogs.

Catalog	Period	Number of Events	Number of Earthquakes with Energy Classes and/or Magnitudes	Number of Non-Earthquakes
ARC	1965–2021	2404	2403	1 *
ARKH	2008–2017	1493	1492	1 *
SHB	2010–2021	2634	2634	0
ISC	1962–2022	16,953	16,937	16
Morozov	1962–2020	4 **	4	0

* According to ISC data. ** Four events with known magnitudes from an additional catalog were included. They were relocated outside the studied area considered in [29], but were within the area studied in the present paper.

The methodology for identifying duplicates when merging catalogs is described in detail in [26]. It was successfully applied to create catalogs of the eastern and western sectors of the Russian Arctic [27,28]. A basic three-parameter model (1) showed efficiency for assessing the proximity between earthquakes. It takes into account the time difference DT , and the epicenter difference in the longitude DX and the latitude DY . After that, the

classification of earthquakes into unique and duplicates is carried out using the threshold value of the metric R_0

$$R_0 = \sqrt{\frac{DT^2}{\sigma_T^2} + \frac{DX^2}{\sigma_X^2} + \frac{DY^2}{\sigma_Y^2}}, \tag{1}$$

where $\sigma_T, \sigma_X, \sigma_Y$ are the standard deviations of time, longitude, and latitude differences between the nearest events from two source catalogs.

3. Results

3.1. Merging Catalogs

As shown in (Table S1, see Supplementary), in the studied region, a significant majority of events are registered by European seismic networks, the data of which are collected in the composite ISC catalog. The number of earthquake records in the ISC catalog is approximately three times greater than the total number of events in the Russian catalogs. Moreover, the data on earthquakes presented in [29] was specified based on the analysis and combination of all available seismic bulletins of Russian and European seismic networks using modern velocity models of the environment. Thus, in the task of merging earthquake catalogs, the following priority sources of earthquake data were chosen (Table 1, Figure 3):

1. Earthquakes from the Morozov catalog (4 events);
2. Earthquakes from the ISC catalog (16,937 events);
3. Earthquakes from catalogs of ARC (2404 events), SBH (2404 events), and ARKH (1493), with preference given to data from the ARC catalog in overlapping areas.

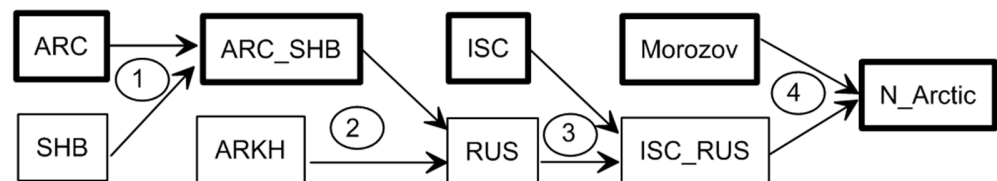


Figure 3. Assembly diagram of the integrated catalog of the studied region. At each stage, the main catalog is marked with a bold frame. The stage numbers are given in ellipses and correspond to Table 2.

Table 2. Scheme and compilation parameters of the integrated catalog.

Stage	Main Catalog	Additional Catalog	Metric Parameters σ_T min, σ_X km, σ_Y km	Threshold Value of the Metric	Estimation of the Number of Errors	Number of Duplicates	Merged Catalog
1	ARC 2403 events	SHB 2634 events	0.054; 22.5; 21.3	12	0.7%	502	ARC_SHB 4535 events
2	ARC_SHB 4535 events	ARKH 1492 events	0.048; 23.9; 22.8	14	0.3%	1136	RUS 4891 events
3	ISC 16,937 events	RUS 4891 events	0.05; 28.3; 24.7	17.5	0.9%	3906	ISC_RUS 17,922 events
4	Morozov 4 events	ISC_RUS 17,922 events				4	N_ARCTICO 17,922

Before the merging process, each of the source catalogs (Table 1) was checked for internal duplicates. Statistical analysis did not reveal any anomalous groups of close events (Figure S3, see Supplementary).

At each stage, the merging of catalogs is performed in two steps. First, the metric parameters (1) are determined. For this, the metric (1) R_0 between the nearest events from two source catalogs with standard parameters $\sigma_T = 0.05$ min, $\sigma_X = \sigma_Y = 15$ km is calculated. The threshold value of the metric $R_0 = 10$ is used for the preliminary duplicate identification, which corresponds to the time and space difference of 0.5 min/150 km.

Standard deviations σ_T , σ_X , and, σ_Y of the variables DT , DX , and DY are calculated for the pre-identified duplicates (Figures 4, 6 and 8). In the next step, a threshold value of the metric is determined and the final duplicate identification takes place (Figures 5, 7 and 9).

The catalogs for the studied region consist of a mixture of data from a large number of agencies. This applies not only to the ISC catalog but also to the ARC catalog, which combines data from several regional networks KOLA, FCIAR, and the GS RAS teleseismic network. In addition, catalogs significantly change over time: the diversity of sources (contributing agencies) and the number of events significantly increase starting from the mid-1990s and then in 2010.

For this reason, metric parameters σ_T , σ_X , and, σ_Y change over time (Figure 8), and heavy tails appear in the distributions of DT , DX , and DY . In this situation, using the methodology applied in [27,28] to determine the threshold value of the metric leads to an increased probability of missing duplicates (Figure S4, see Supplementary). Therefore, in this paper, it was decided not to use a multivariate normal distribution model. Instead, the sampling distribution (without modeling by the normal distribution, as in the original method) of the metric for the nearest events from the two merged catalogs is used.

We assume that the maximum value of the metric for events that can be duplicates is $R_0 = 30$, which corresponds to a time and space difference of about 1.5 min and 600 km. We construct the distribution of such events F_{dub} . The red lines in Figures 5b, 7b and 9b represent the value of $1 - F_{dub}$, which we consider as the probability of missing a duplicate (error of the first kind). The probability of a false duplicate (error of the second kind) is estimated in the same way as in [27,28]. For this, we calculate the values of the metric (1) R_0 between events within an additional catalog. The blue lines in Figures 5b, 7b and 9b represent the proportion of events with a proximity less than a given value of R_0 . The black lines show the estimate of the total probability of the first and the second kind errors. The threshold value of the metric minimizes the total number of errors. Figures 5c, 7c, and 9c show the distribution of normalized times and distances for the nearest events from the merged catalogs. The metric contour lines correspond to the chosen threshold value, which provides the optimal separation of duplicates and unique events.

The numerical parameters of the catalog merging are given in Table 2. The integrated catalog contains 17,922 events.

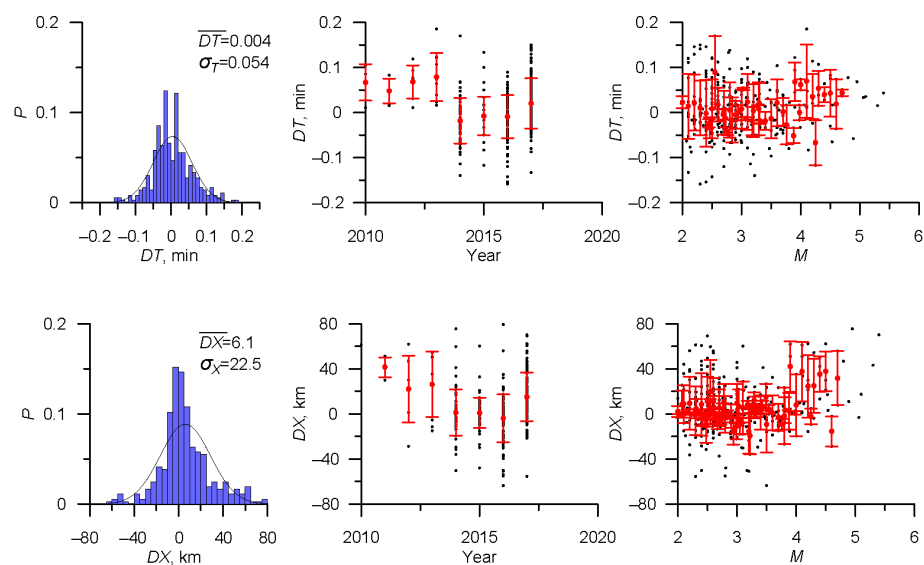


Figure 4. Cont.

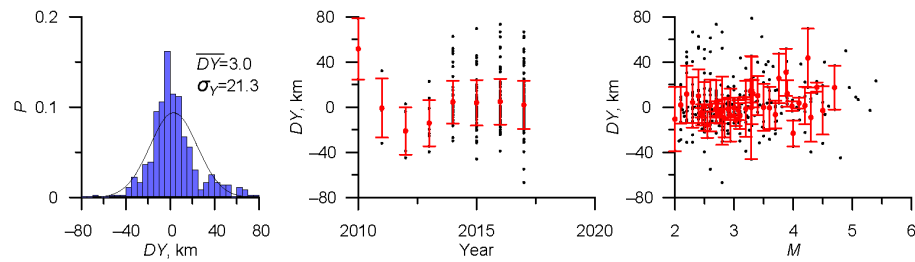


Figure 4. Stage 1. Determination of numerical parameters of the metric (1) for merging the ARC and SHB catalogs. Distributions of variables DT , DX , DY , and the dependence of dispersion and mean values on time and magnitude of events.

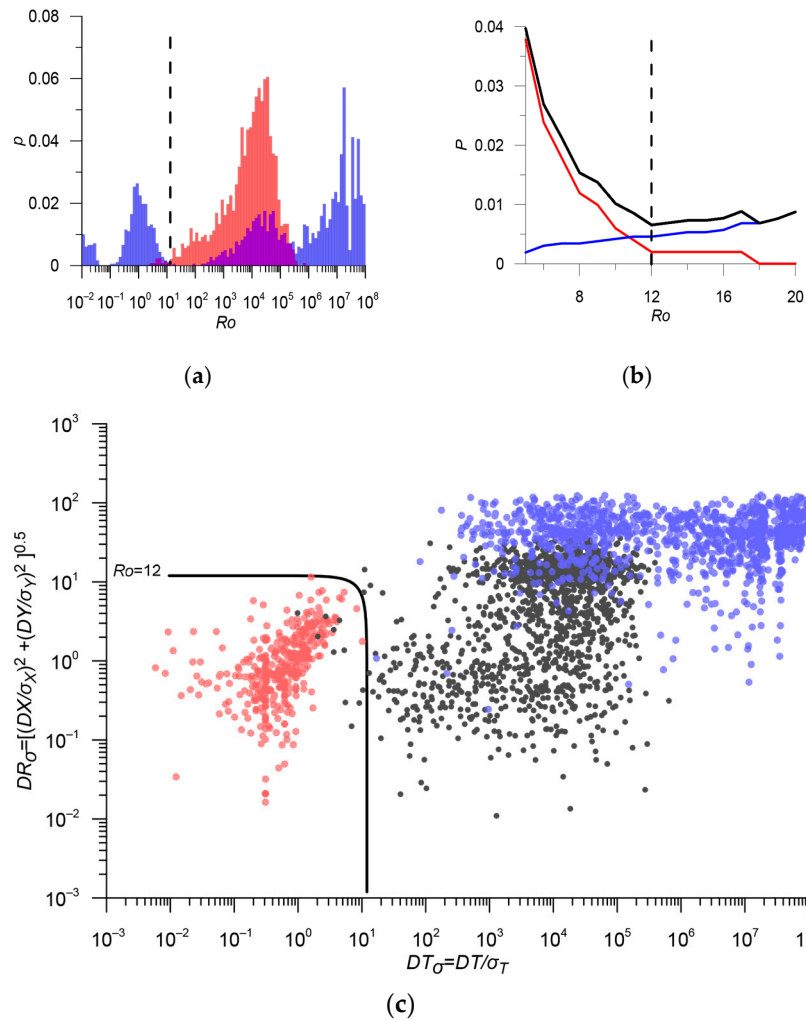


Figure 5. Stage 1: Merge of catalogs ARC and SHB. (a) Comparison of the metric distribution ARC/SHB pairs (blue histogram) and the same metric for SHB/SHB earthquakes (red histogram); (b) Threshold optimization: the red line shows the probability of missing a duplicate, the blue line shows the probability of a false duplicate, and the black line shows the total probability of the first and the second kind errors. The threshold value $R_o = 12$, which minimizes the total number of errors, approximately 0.7%, is shown by a dashed line; (c) Distribution of normalized DT and DR , and the contour line of metric (1). Colored dots represent ARC/SHB pairs (pink dots are duplicates, blue dots are unique events), and black dots are distances between SHB/SHB events in metric (1). The values of the metric for earthquakes in the SHB catalog are significantly larger than for ARC/SHB duplicates (pink dots). The contour line of the metric (1) $R_o = 12$ provides close to optimal separation of duplicates and naturally grouped events. Absolute duplicates are not shown.

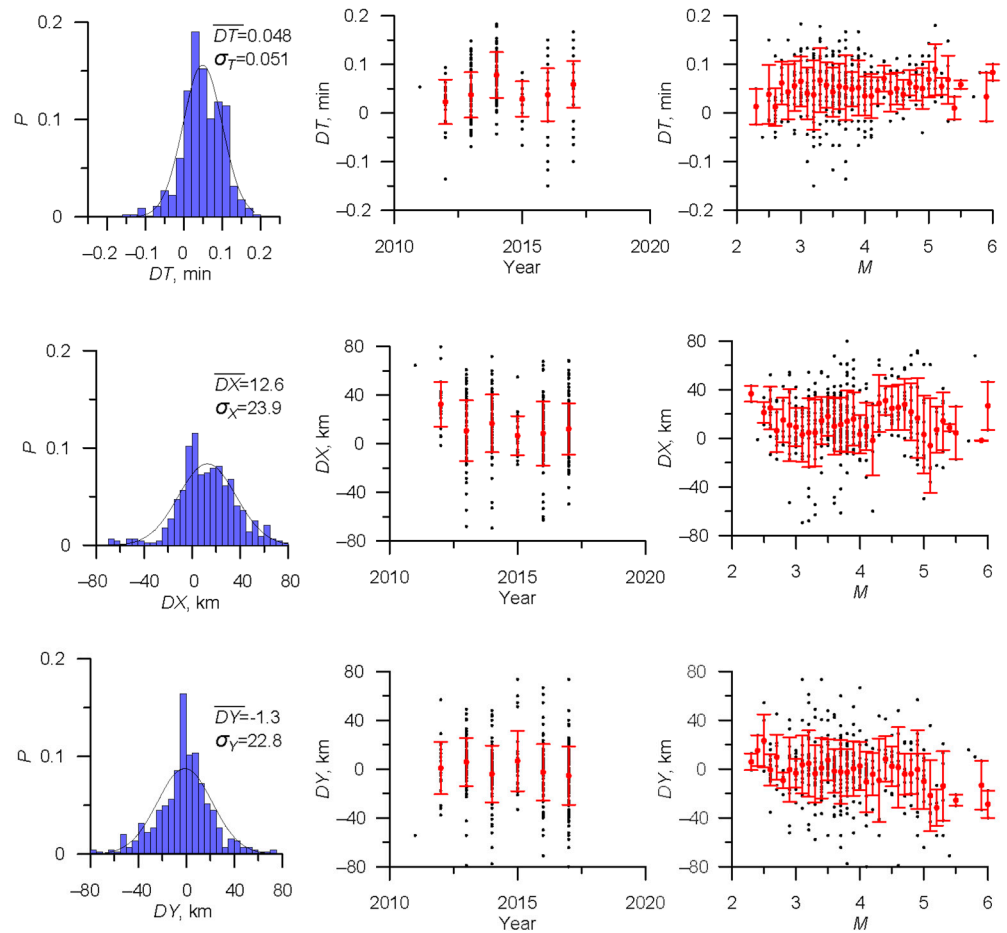


Figure 6. Determination of numerical parameters of the metric (1) for merging the ARC_SHB and ARKH catalogs. Distributions of variables DT , DX , DY , and the dependence of dispersion and mean values on time and magnitude of events.

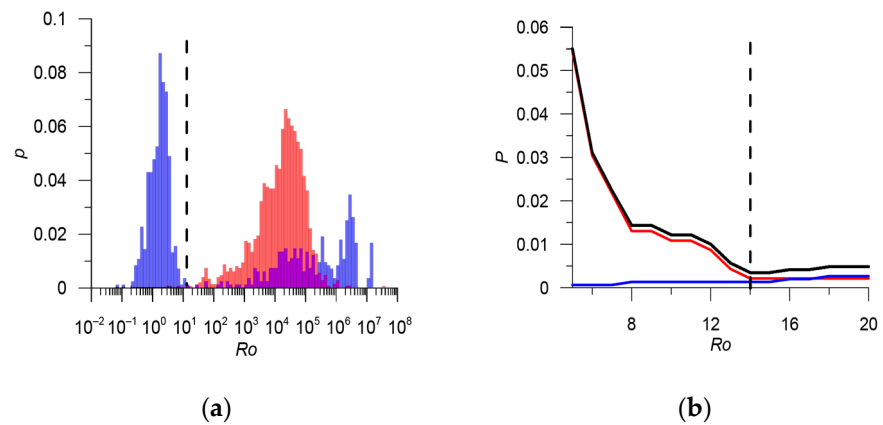


Figure 7. Cont.

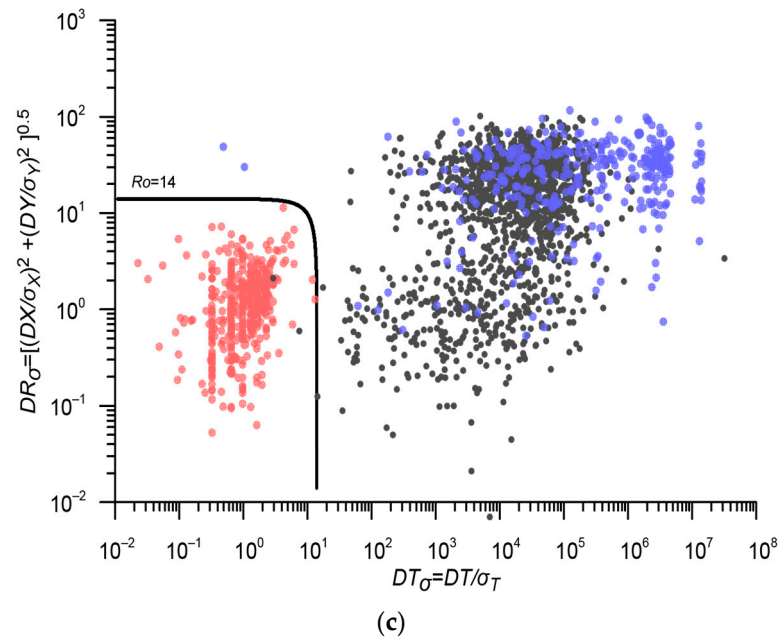


Figure 7. Stage 2: Merge of catalogs ARC_SHB and ARKH. (a) Comparison of the metric distribution ARC_SHB/ARKH pairs (blue histogram) and the same metric for ARKH/ARKH earthquakes (red histogram); (b) Threshold optimization: the red line shows the probability of missing a duplicate, the blue line shows the probability of a false duplicate, and the black line shows the total probability of the first and the second kind errors. The threshold value $R_0 = 12$, which minimizes the total number of errors, approximately 0.7%, is shown by a dashed line; (c) Distribution of normalized DT and DR , and the contour line of metric (1). Colored dots represent ARC_SHB/ARKH pairs (pink dots are duplicates, blue dots are unique events), and black dots are distances between ARKH/ARKH events in metric (1). The values of the metric for earthquakes in the ARKH catalog are significantly larger than for ARC_SHB/ARKH duplicates (pink dots). The contour line of the metric (1) $R_0 = 12$ provides close to optimal separation of duplicates and naturally grouped events. Absolute duplicates are not shown.

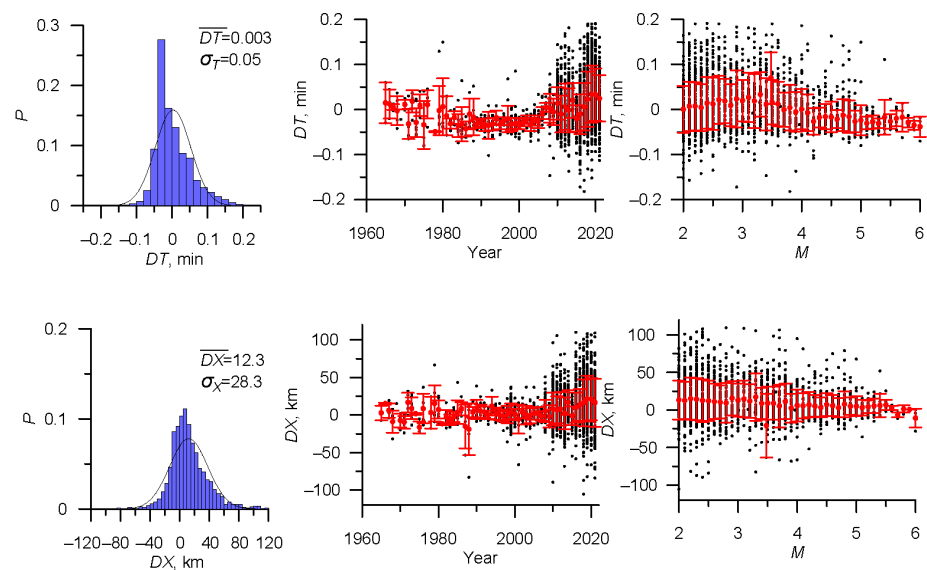


Figure 8. Cont.

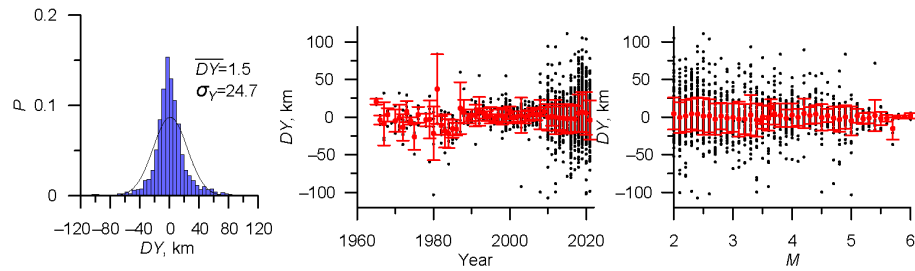


Figure 8. Stage 3. Determination of numerical parameters of the metric (1) for merging the ISC and RUS catalogs. Distributions of variables DT , DX , DY , and the dependence of dispersion and mean values on time and magnitude of events.

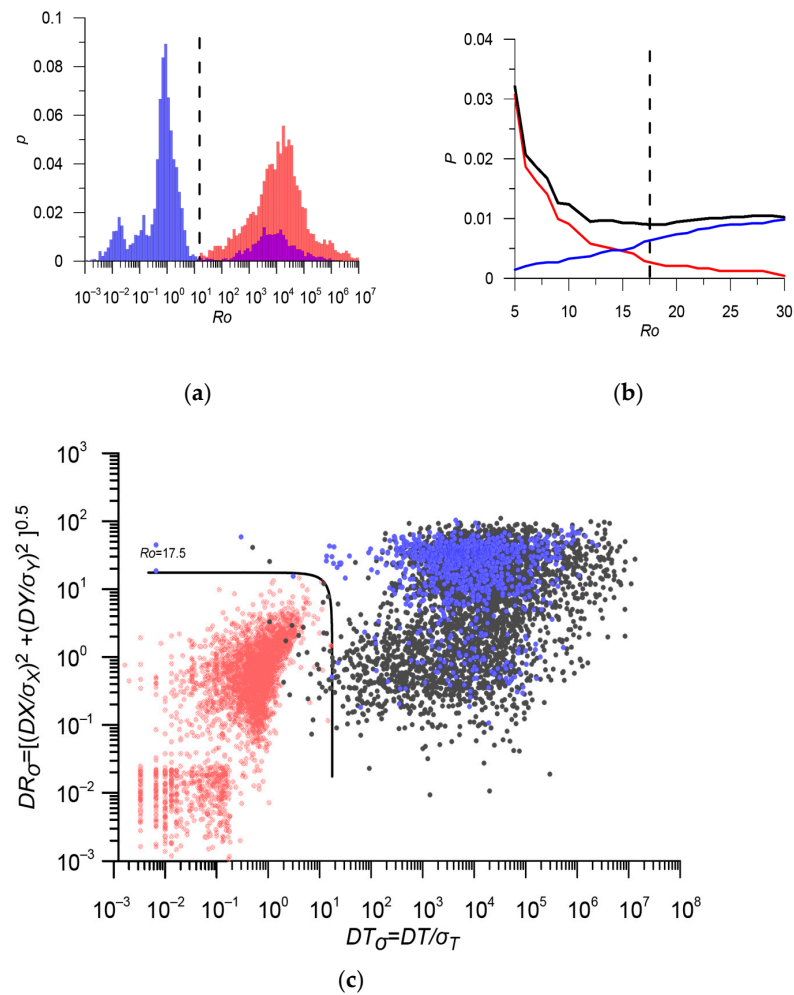


Figure 9. Stage 3: Merge of catalogs ISC and RUS. (a) Comparison of the metric distribution ISC/RUS pairs (blue histogram) and the same metric for RUS/RUS earthquakes (red histogram); (b) Threshold optimization: the red line shows the probability of missing a duplicate, the blue line shows the probability of a false duplicate, and the black line shows the total probability of the first and the second kind errors. The threshold value $Ro = 12$, which minimizes the total number of errors, approximately 0.7%, is shown by a dashed line; (c) Distribution of normalized DT and DR , and the contour line of metric (1). Colored dots represent ISC/RUS pairs (pink dots are duplicates, blue dots are unique events), and black dots are distances between RUS/RUS events in metric (1). The values of the metric for earthquakes in the RUS catalog are significantly larger than for ISC/RUS duplicates (pink dots). The contour line of the metric (1) $Ro = 12$ provides close to optimal separation of duplicates and naturally grouped events. Absolute duplicates are not shown.

3.2. Magnitude Unification in the Integrated Earthquake Catalog

During the second stage of creating the integrated earthquake catalog, the magnitude unification of events was carried out. The integrated catalog contains multiple definitions of the magnitude of different types from various agencies. Different magnitudes are presented in different periods and different parts of the considered region. A preliminary study showed that some magnitude estimates significantly changed over time: ML^{NAO} magnitude changed in 2009, MD^{BER} magnitude changed in 2010, and ML^{DNK} magnitude changed in 2015 (Figure 10).

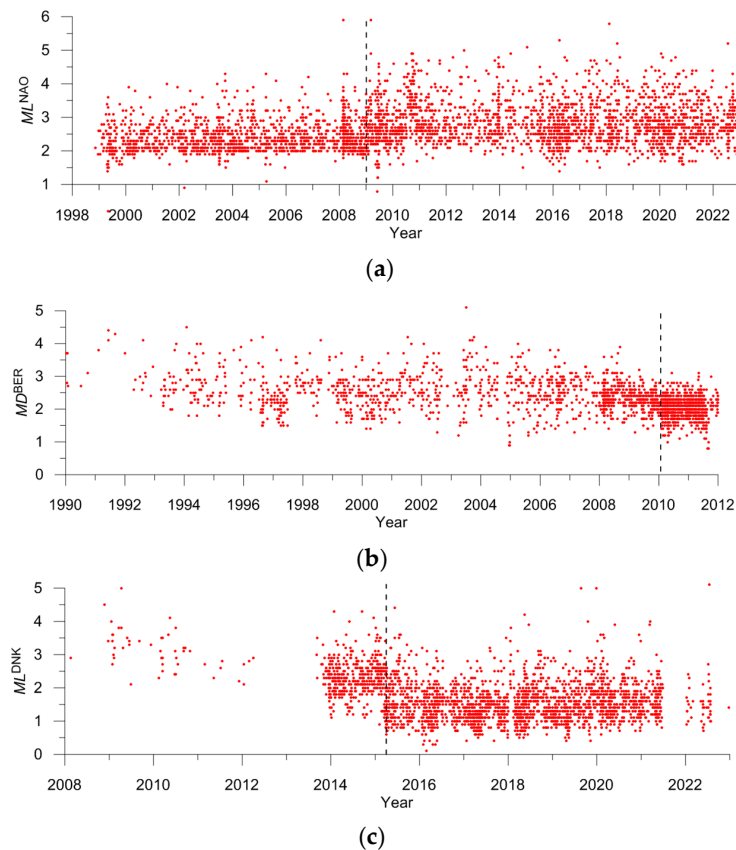


Figure 10. Change in magnitude estimates in time: (a) ML^{NAO} ; (b) MD^{BER} ; (c) ML^{DNK} .

Moreover, we assumed that the magnitude ratio may vary in different seismically active zones. We identified three sub-regions: Svalbard, Knipovich Ridge, and Gakkel Ridge (Figure 2). Magnitude unification was independently performed in these three sub-regions.

As the reference scale, we chose the magnitude based on the seismic moment determined by GCMT. We analyzed correlation ratios between various magnitudes and proposed conversion formulas for obtaining “proxy- MW ” estimates. We used a simple shift-type ratio $M = m + a$ for almost all magnitudes, except for surface wave magnitudes MS^{ISC} , MS^{MOS} , and MLH^{GSR} , for which linear ratios were used.

3.2.1. Svalbard

The catalog of the Svalbard sub-region contains 6921 events. The magnitude MW^{GCMT} is determined for only 6 events, while the magnitudes mb^{ISC} , mb^{NEIC} are known for 153 events. The magnitude $mb^{\text{ISC}} \approx MW^{\text{GCMT}}$ (Figure 11a). This corresponds to the practice of ISC that uses mb as a proxy- MW for earthquakes with $M < 5.0$ [32]. This significantly increases statistics and expands the magnitude range for converting other magnitudes to proxy- MW . Most events (5927) have a local magnitude ML^{BER} . In total, about 88% of events have MW^{GCMT} , $mb^{\text{ISC, NEIC}}$, and ML^{BER} magnitudes. We consider the ratios between these magnitudes as basic (Figure 11). For the remaining magnitudes, we built ratios with

mb^{ISC} and ML^{BER} . Regressions with mb^{ISC} and ML^{BER} for most magnitudes are very close (Figures 12 and 13). This confirms the hypothesis of linearity in the ratio between different estimates over a wide range of magnitudes. The exception is the MD^{BER} magnitude in 2010–2011, for which magnitude estimates for 34 events, where other determinations are absent, were considered unreliable. For 12 events, the ratios were poorly determined due to the small number of events with both magnitude determinations (Figure 14). For 16 events, the ratios were not determined. In total, the unified magnitude was poorly determined for less than 1% of events. Statistics and formulas for converting magnitudes in the Svalbard sub-region are presented in Table 3.

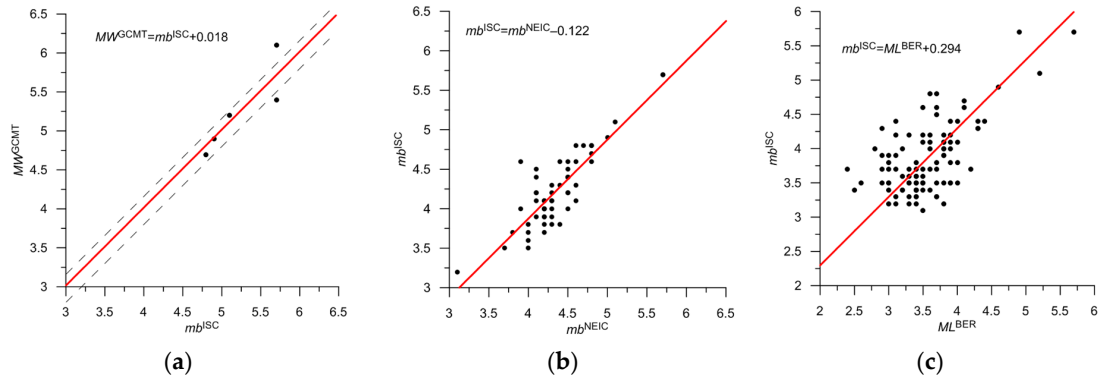


Figure 11. Basic shift-type correlation ratios for magnitudes MW^{GCMT} , $mb^{ISC,NEIC}$, and ML^{BER} in the sub-region of Svalbard. Dashed lines in (a) show 95% confidence interval, in (b) and (c), 95% confidence intervals are not shown since they are less than 0.1.

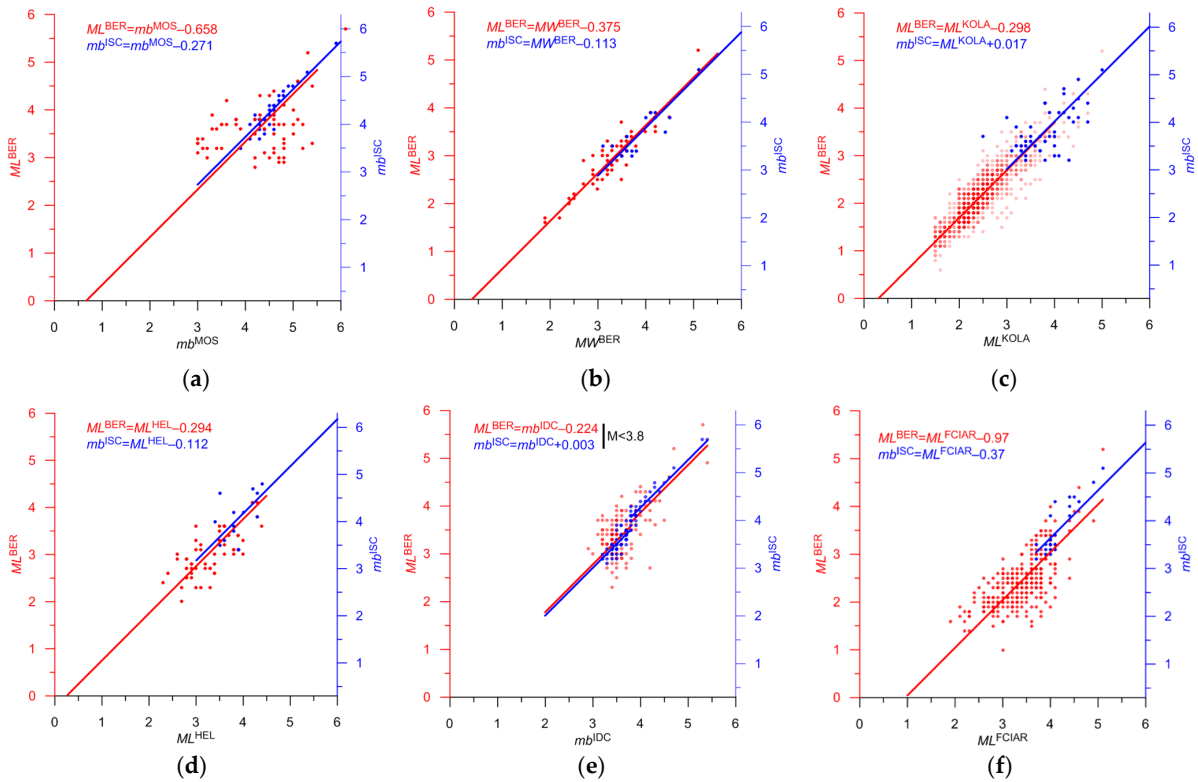


Figure 12. Shift-type correlation ratios for different magnitudes with mb^{ISC} (blue), and ML^{BER} (red) in the sub-region of Svalbard. Y-axis for mb^{ISC} is shifted to 0.3 in accordance with the ratio between mb^{ISC} and ML^{BER} in Svalbard (Table 4 and Figure 11). Dots are observations, lines are the best shift-type fits. The 95% confidence intervals are not shown since they are less than 0.1.

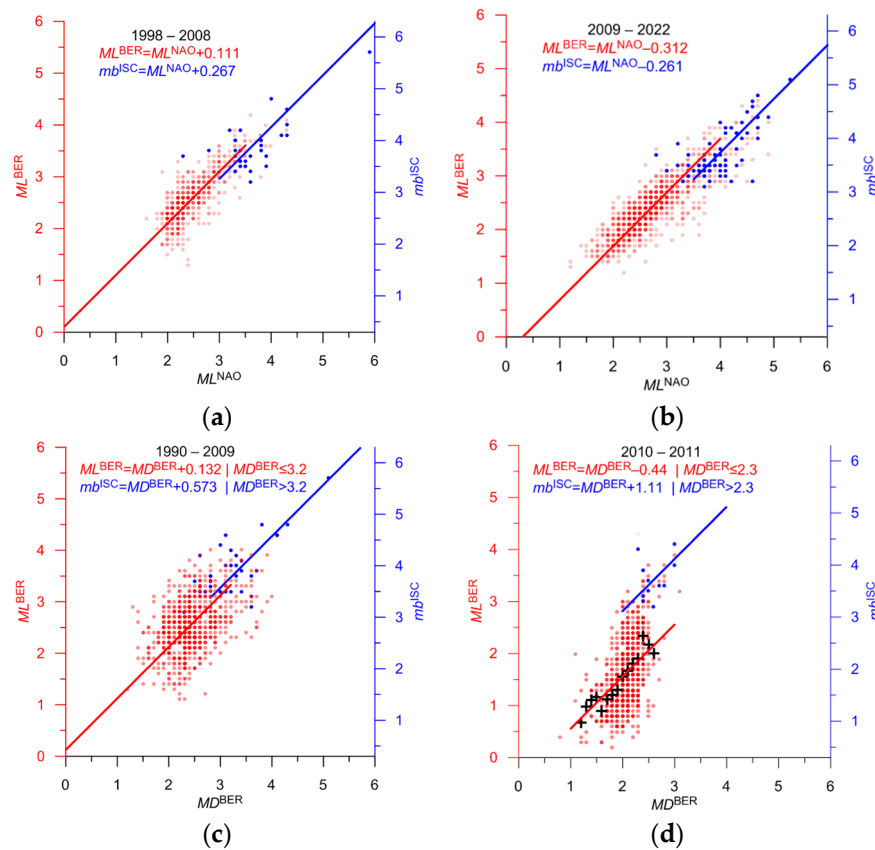


Figure 13. Shift-type correlation ratios for ML^{NAO} and MD^{BER} magnitudes with mb^{ISC} (blue), and ML^{BER} (red) in the sub-region of Svalbard in the different periods. Black crosses in (d) are the population mean of ML^{BER} . The Y-axis for mb^{ISC} is shifted to 0.3 in accordance with the ratio between mb^{ISC} and ML^{BER} . Dots are observations, lines are the best shift-type fits. The 95% confidence intervals are not shown since they are less than 0.1.

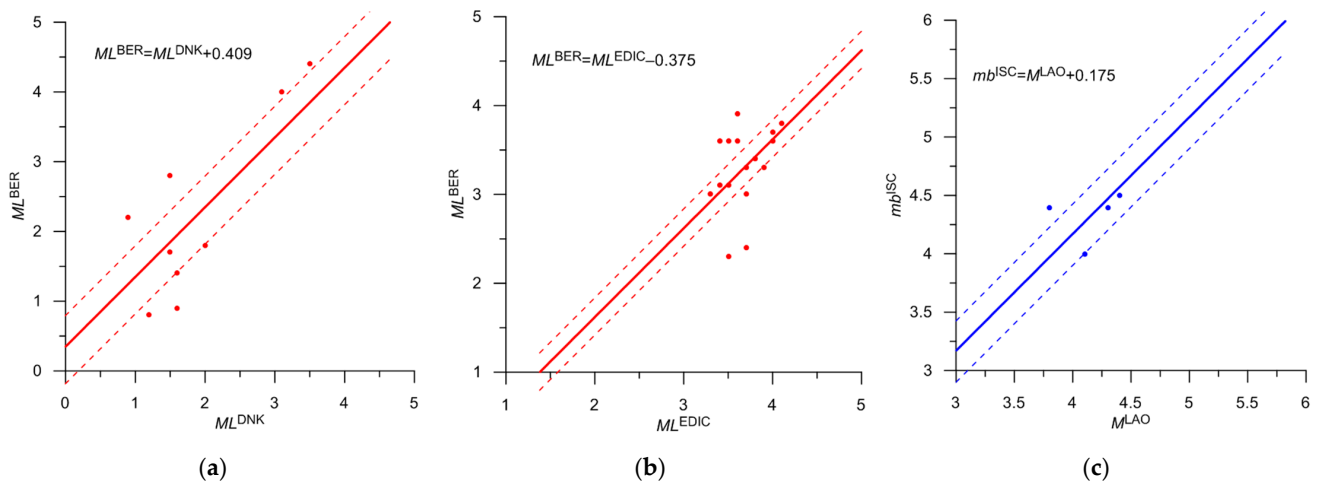


Figure 14. Shift-type correlation ratios for different magnitudes in the sub-region of Svalbard. Correlations are unreliable due to a small amount of data. Correlations with mb^{ISC} and ML^{BER} are shown in blue and red, respectively. Dots are observations, lines are the best shift-type fits. Dashed lines show a 95% confidence interval.

Table 3. Magnitude in the integrated catalog: Svalbard.

Agency	Type of Magnitude	Priority	Number of Events	Magnitude in the Integrated Catalog	Correlation	Figure	Mmin—Mmax. Initial Magnitude Scale	Note
GCMT	<i>MW</i>	1	6	$M = MW^{GCMT}$			4.7–6.1	
ISC	<i>mb</i>	2	130	$M = mb^{ISC}$	0.78	11a	3.1–5.6	
NEIC, NEIS	<i>mb</i>	2	17	$M = mb^{NEIC} - 0.1$	0.75	11b	3.3–4.9	
BER	<i>ML</i>	3	5927	$M = ML^{BER} + 0.3$	0.39	11c	0.3–3.9	
KOLA	<i>ML</i>	4	330	$M = ML^{KOLA}$	0.79	12c	1.4–3.4	
NAO	<i>ML</i>	4	250	$M = ML^{NAO} + 0.4$	0.65	13a	0.9–3.2	1998–2008
NAO	<i>ML</i>	4	47	$M = ML^{NAO}$	0.53	13b	1.2–3.5	2009–2022
FCIAR	<i>ML</i>	4	46	$M = ML^{FCIAR} - 0.7$	0.47	12f	1.8–3.8	
BER	<i>MD</i>	4	92	$M = MD^{BER} + 0.4$	0.43	13c	0.9–3.2	1990–2009
BER	<i>MD</i>	5	34	$M = MD^{BER} - 0.1$	0.25	13d	0.8–2.3	2010–2011 unreliable, Non-linear relation
MOS	<i>mb</i>	4	2	$M = mb^{MOS} - 0.3$	0.89	12a	4.9–5.8	
BER	<i>Mw</i>	4	7	$M = Mw^{BER} - 0.1$	0.85	12b	3.1–3.9	
HEL	<i>ML</i>	4	4	$M = ML^{HEL}$	0.53	12d	2.3–3.2	
IDC	<i>mb</i>	4	1	$M = mb^{IDC}$	0.78	12e	3.5	
DNK	<i>ML</i>	5	3	$M = ML^{DNK} + 0.7$	0.66	14a	1.8–2.0	Poorly determined
EDIC	<i>ML</i>	5	7	$M = ML^{EDIC} - 0.1$	0.20	14b	2.8–4.0	Poorly determined
LAO	<i>M</i>	5	2	$M = M^{LAO} + 0.2$	0.07	14c	3.4–3.8	Poorly determined
NAO	<i>mb</i>	5	1	$M = mb^{NAO}$			4	Not Determined
HEL	<i>MD</i>	5	5	$M = MD^{HEL}$			3.2–4.0	Not Determined
BER	<i>mb(Pn)</i>	5	4	$M = mb(Pn)^{BER}$			2.5–2.8	Not Determined
WAR	<i>M</i>	5	5	$M = M^{WAR}$			2.1–3.0	Not Determined
NUR	<i>M</i>	5	1	$M = M^{NUR}$			3.9	Not Determined
Total			6921					

3.2.2. Knipovich and Gakkel Ridges

The Gakkel and Knipovich ridges are structures of a similar tectonic type, known as “mid-ocean ridges”. Preliminary analysis of the ratio of different magnitudes, for which there are sufficient statistics in both ridges, shows that most of the ratios are very similar. Figure 15a,b show the ratios for MW^{GCMT} and mb^{ISC} , mb^{NEIC} . In many cases, we construct ratios based on combined data from the Gakkel and Knipovich ridges. The ratios were found to be different for ML^{FCIAR} . For some magnitude types in the Gakkel Ridge, there are insufficient statistics, and the ratios from the Knipovich Ridge were used, which we considered unreliable. Detailed statistics are separately presented for the Knipovich and Gakkel ridges.

The catalog for the Knipovich Ridge sub-region contains 8912 events. The MW^{GCMT} magnitude is determined for 112 events, while magnitudes mb^{ISC} and mb^{NEIC} are known for 885 events. Magnitude $MW^{GCMT} \approx mb^{ISC} + 0.2$ (Figure 15a). A large number of events have magnitudes of ML^{BER} (2974), Mw^{BER} (1892), $mb(Pn)^{BER}$ (1521), and $M = ML^{DNK}$ (2602), which together make up over 92% of events. The ratios between MW^{GCMT} , mb^{ISC} , mb^{NEIC} , and ML^{BER} magnitudes are considered basic (Figure 15). For other magnitudes, the ratios are constructed with MW^{GCMT} , mb^{ISC} , and ML^{BER} when there are sufficient statistics. As in the Svalbard region, regressions with MW^{GCMT} , mb^{ISC} , and ML^{BER} for most magnitudes are very close (Figures 16 and 17). This confirms the hypothesis of linearity in the ratio between different estimates over a wide range of magnitudes. The exception is the magnitude

MD^{BER} in 2011–2012, where estimates for 20 events with no other determinations were considered unreliable. Ratios for 16 events were poorly determined due to small statistics (Figure 18). Ratios for 11 events were not determined. In total, the unified magnitude was poorly determined for less than 1% of events. Statistics and formulas for converting magnitudes in the Knipovich Ridge sub-region are presented in Table 4.

Table 4. Magnitude in the integrated catalog: Knipovich Ridge.

Agency	Type of Magnitude	Priority	Number of Events	Magnitude in the Integrated Catalog	Correlation	Figure	Mmin—Mmax. Initial Magnitude Scale	Note
GCMT	<i>MW</i>	1	112	$M = MW^{GCMT}$		–	4.6–6.7	
ISC	<i>mb</i>	2	805	$M = mb^{ISC} + 0.2$	0.67	15a	2.9–6.3	Gakkel and Knipovich
NEIC, NEIS	<i>mb</i>	2	80	$M = mb^{NEIC} + 0.1$	0.66	15b	3.3–4.9	Gakkel and Knipovich
BER	<i>ML</i>	3	2974	$M = ML^{BER} + 1.2$	0.54	15c	0.3–3.7	Knipovich
BER	<i>Mw</i>	4	1892	$M = Mw^{BER} - 0.1$	0.72	16a	1.3–5.0	Gakkel and Knipovich
BER	<i>mb(Pn)</i>	4	1521	$M = mb(Pn)^{BER} - 0.1$	0.82	16b	1.7–4.6	Gakkel and Knipovich
DNK	<i>ML</i>	4	83	$M = ML^{DNK} + 0.6$	0.79	16c	0.9–3.1	2008–2015.2 Knipovich
DNK	<i>ML</i>	4	753	$M = ML^{DNK} + 1.3$	0.57	16d	0.1–3.1	2015.3–2022 Knipovich
KOLA	<i>ML</i>	4	82	$M = ML^{KOLA} + 0.5$	0.65	16e	1.3–3.4	Knipovich
NAO	<i>ML</i>	4	265	$M = ML^{NAO} + 1.1$	0.53	16f	0.2–3.4	1990–2008 Gakkel and Knipovich
NAO	<i>ML</i>	4	32	$M = ML^{NAO} + 0.4$	0.69	16g	1.7–4.2	2009–2022 Gakkel and Knipovich
FCIAR	<i>ML</i>	4	102	$M = ML^{FCIAR}$	0.42	16h	2.3–4.1	Knipovich
BER	<i>MD</i>	5	96	$M = MD^{BER} + 1.1$	0.62	17a	1.5–4.4	1990–2009 Knipovich
BER	<i>MD</i>	5	20	$M = MD^{BER} + 0.8 \mid MD < 2.7$	0.23	17b	1.5–2.5	2010–2011 Knipovich, unreliable
IDC	<i>mb</i>	4	21	$M = mb^{IDC} + 0.2$	0.85	17c	3.0–3.6	Gakkel and Knipovich
EIDC	<i>mb</i>	4	11	$M = mb^{EIDC} + 0.3$	0.76	17d	2.9–3.7	Gakkel and Knipovich
USCGS	<i>mb</i>	4	4	$M = mb^{USCGS} + 0.2$	0.83	18a	4.2–4.6	Gakkel and Knipovich
MOS	<i>MS</i>	4	1	$M = 0.515MS^{ISC} + 2.88$	0.71	18d	4.7	Gakkel and Knipovich
NAO	<i>mb</i>	4	3	$M = mb^{NAO} + 0.5$	0.62	18b	3.6–4.1	Knipovich
HFS	<i>mb</i>	4	1	$M = mb^{NAO} + 0.5$	0.50	18c	3.9	Knipovich
OTT	<i>ML</i>	4	27	$M = ML^{OTT} + 0.1$	0.23	18e	3.2–5.0	Gakkel and Knipovich
EIDC	<i>ML</i>	5	7	$M = ML^{EIDC} + 0.2$	0.05	18h	3.4–4.2	Poorly determined
BER	<i>Mc</i>	5	3	$M = Mc^{BER} + 0.4$	0.03	18f	1.7–3.2	Poorly determined
DNK	<i>Mc</i>	5	6	$M = Mc^{BER} - 0.5$	0	18g	2.1–3.7	Poorly determined
CGS	<i>M</i>	5	5	$M = M^{CGS}$			4.2–4.7	Not Determined
DNK	<i>MD</i>	5	1	$M = MD^{BER}$			2.4	Not Determined
PAL	<i>M</i>	5	2	$M = M^{PAL}$			4.3	Not Determined
STU	<i>M</i>	5	1	$M = M^{STU}$			5.2	Not Determined
OTT	<i>Mn</i>	5	1	$M = Mn^{OTT}$			3.1	Not Determined
WAR	<i>M</i>	5	1	$M = M^{WAR}$			2.6	Not Determined
Total			8912					

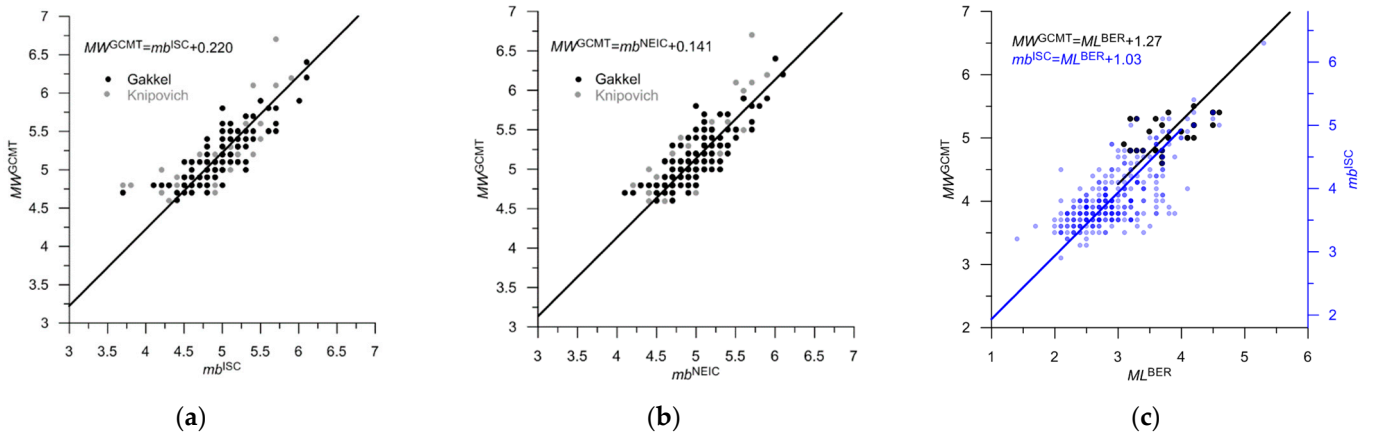


Figure 15. Basic shift-type correlation ratios for magnitudes MW^{GCMT} , mb^{ISC} , $NEIC$, and ML^{BER} in the sub-region of Knipovich Ridge. Ratios (a,b) are constructed using Knipovich (gray dots) and Gakkel (black dots) ridges data. In (c), correlations of ML^{BER} with mb^{ISC} (blue) and MW^{GCMT} (black) are very similar. The Y-axis for mb^{ISC} is shifted to 0.2 in accordance with the ratio between mb^{ISC} and MW^{GCMT} shown in (a). Dots are observations, lines are the best shift-type fits. The 95% confidence intervals are not shown since they are less than 0.1.

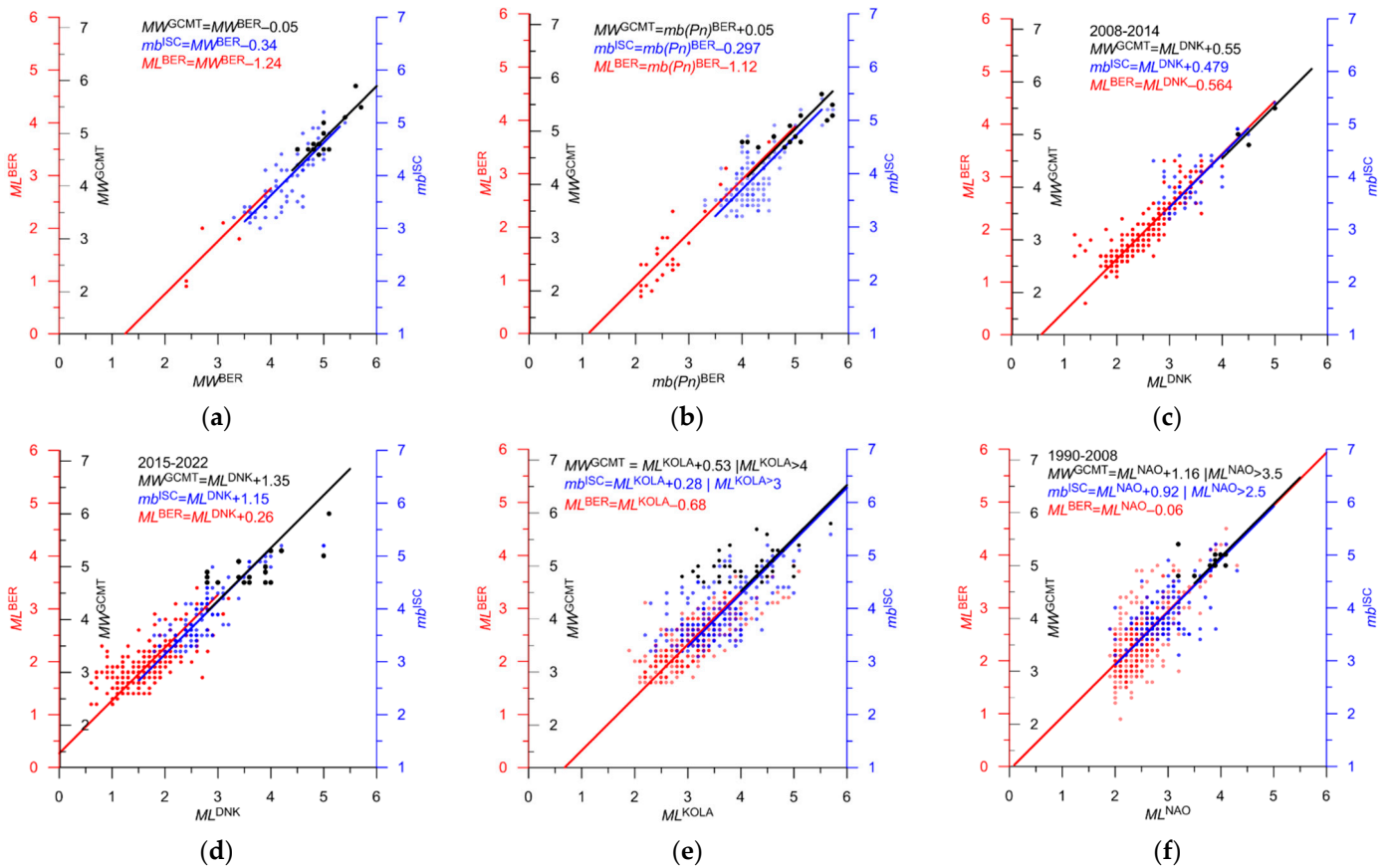


Figure 16. Cont.

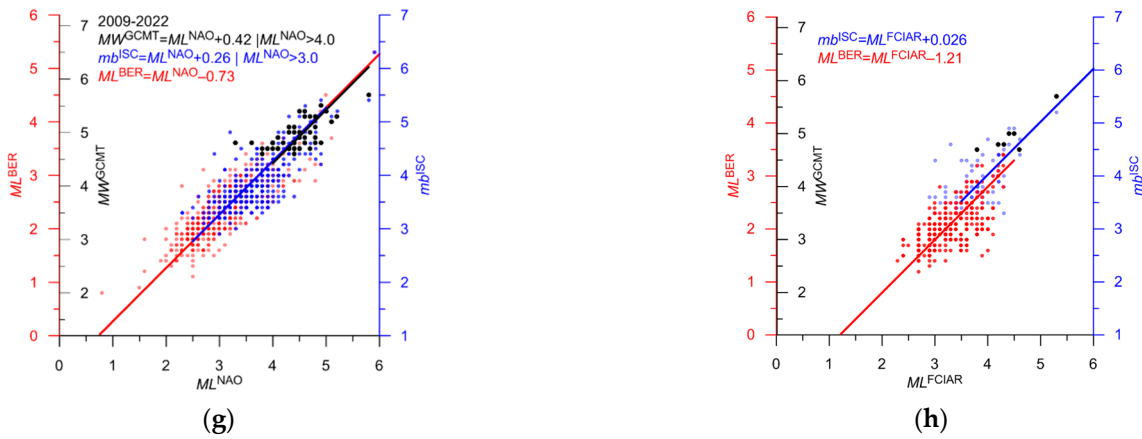


Figure 16. Correlation ratios for different magnitudes with MW^{GCMT} (black), mb^{ISC} (blue), and ML^{BER} (red) in the sub-region of Knipovich Ridge. The Y-axes for MW^{GCMT} , mb^{ISC} and ML^{BER} are shifted relative to each other in accordance with the basic ratio between the magnitudes shown in Figure 15. Dots are observations, lines are the best shift-type fits. The 95% confidence intervals are not shown since they are less than 0.1.

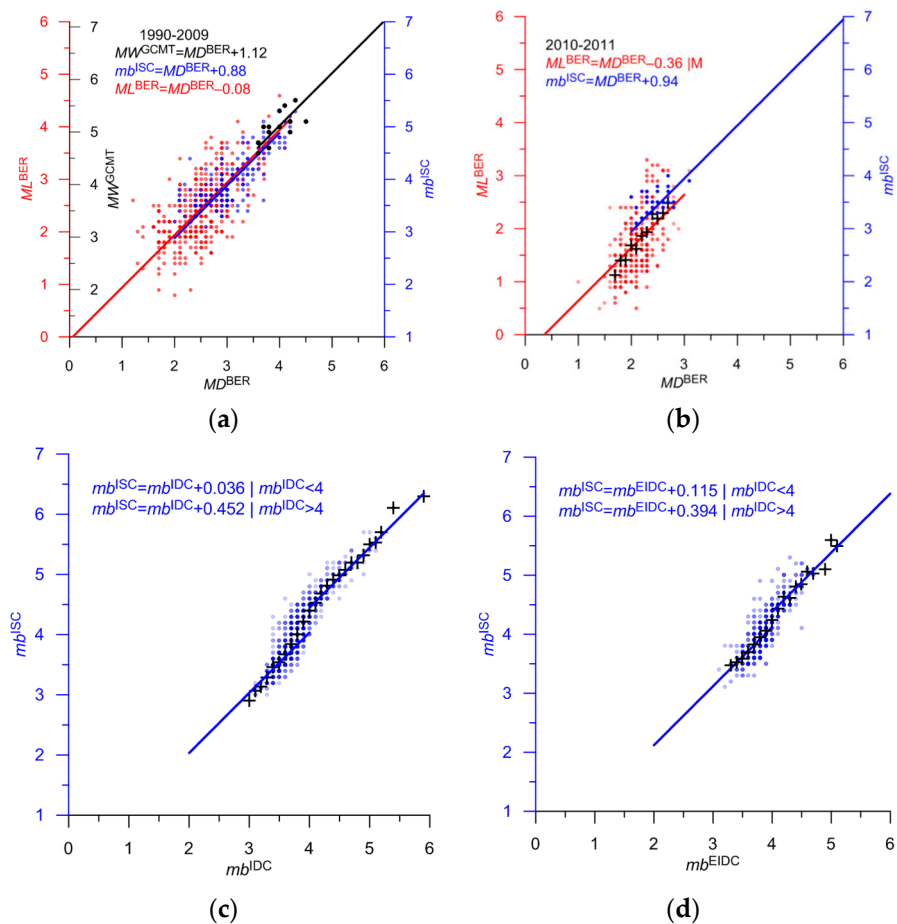


Figure 17. Correlation ratios for MD^{BER} and mb^{IDC} , mb^{EIDC} with MW^{GCMT} (black), mb^{ISC} (blue), and ML^{BER} (red) in the sub-region of Knipovich Ridge. Y-axes for MW^{GCMT} , mb^{ISC} and ML^{BER} are shifted relative to each other in accordance with the basic ratio between the magnitudes shown in Figure 15. Black crosses in (b–d) are the population mean of ML^{BER} and mb^{ISC} . Ratios for mb^{IDC} mb^{EIDC} are constructed using the Knipovich and Gakkel ridges data. Dots are observations, lines are the best shift-type fits. The 95% confidence intervals are not shown since they are less than 0.1.

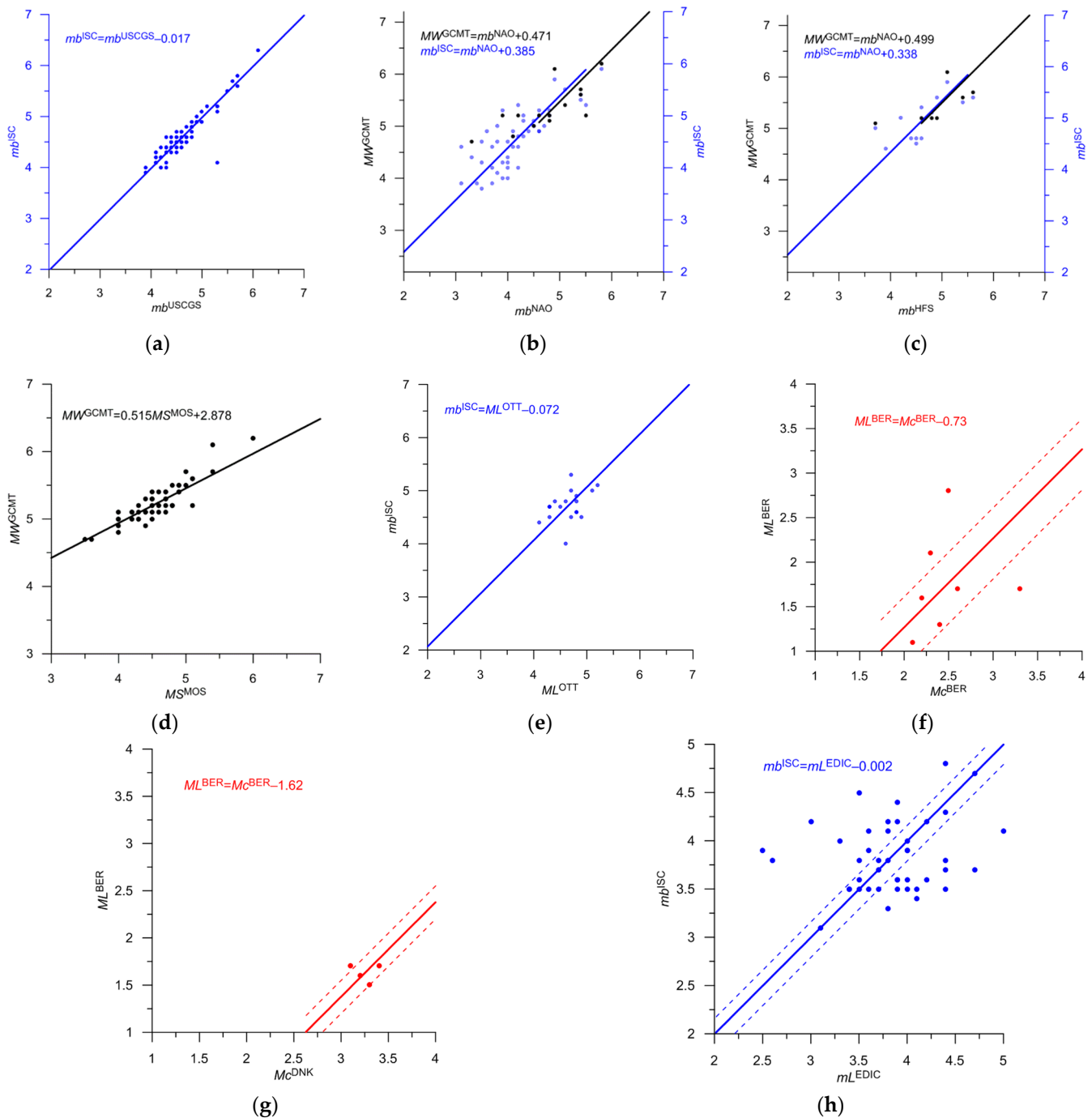


Figure 18. Correlation ratios for various magnitudes with MW^{GCMT} (black), $mb^{ISC, NEIC}$ (blue), and ML^{BER} (red) in the sub-region of Knipovich Ridge. Y-axes in (b,c) for MW^{GCMT} , mb^{ISC} are shifted relative to each other in accordance with the basic ratio between the magnitudes shown in Figure 15. All ratios are shift type, excluding MS^{MOS} (d), where we use linear relation. Dots are observations, lines are the best fits. Ratios are constructed using the Knipovich and Gakkel ridges data. Ratios (f–h) are poorly determined, and dashed lines show 95% confidence intervals.

The catalog of the Gakkel Ridge sub-region contains 2089 events. The magnitude MW^{GCMT} is determined for 138 events, while the magnitudes mb^{ISC} and mb^{NEIC} are known for 1053 events. A large number of earthquakes (561) have a ML^{FCIAR} magnitude, accounting, together with MW^{GCMT} , mb^{ISC} , and mb^{NEIC} , for almost 84% of the events. The magnitude $MW^{GCMT} \approx mb^{ISC} + 0.2$ (Figure 15a). The magnitude ratios, only using events from the Gakkel Ridge, are shown in Figure 19. We constructed ratios with MW^{GCMT} and mb^{ISC} . The

ML^{FCIAR} magnitude was not used due to insufficient statistics (for most events with ML^{FCIAR} , it is the only determined magnitude). For local magnitudes ML^{BER} , ML^{DNK} , and ML^{KOLA} (a total of 45 events), ratios obtained for the Knipovich Ridge events were used, but we considered them unreliable. For 21 events, the ratios were poorly determined due to the small statistics (Figures 18e and 19h). For seven events, the ratios were not determined. In total, the unified magnitude was poorly determined for 3.5% of the events. Statistics and formulas for converting magnitudes in the Gakkel Ridge sub-region are given in Table 5.

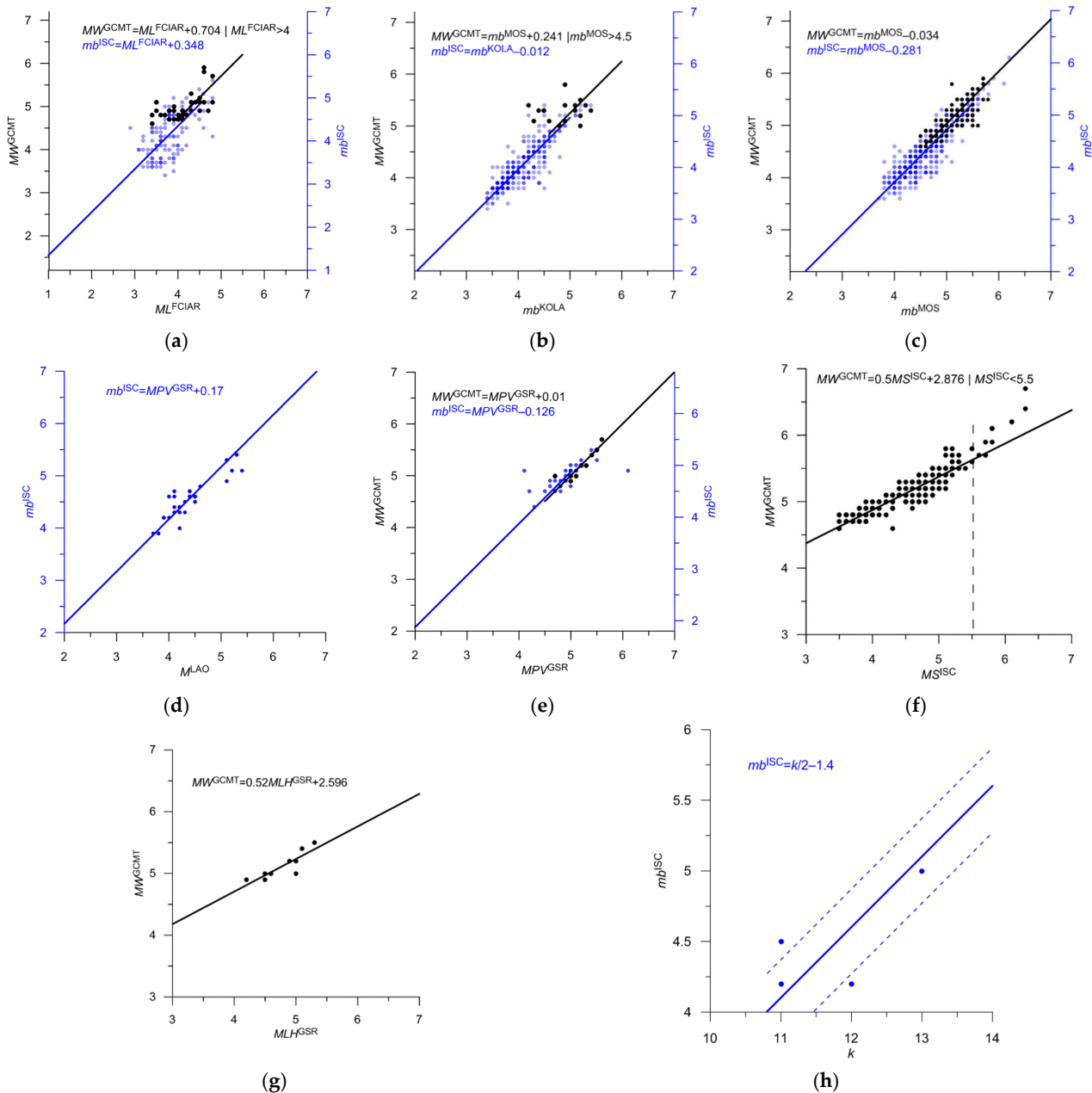


Figure 19. Correlation ratios for various magnitudes with MW^{GCMT} (black), and mb^{ISC} (blue) in the sub-region of Gakkel Ridge. Y-axes for MW^{GCMT} , mb^{ISC} in (a–c,e) are shifted relative to each other in accordance with the basic ratio between the magnitudes shown in Figure 15. All ratios are shift type, excluding MS^{ISC} (f) and MLH^{GSR} (g), where we use linear relation. Dots are observations, lines are the best fits. The ratio (h) is poorly determined, and dashed lines show 95% confidence intervals. Intervals are not shown in (a–g) since they are less than 0.1.

Table 5. Magnitude in the integrated catalog: Gakkel Ridge.

Agency	Type of Magnitude	Priority	Number of Events	Magnitude in the Integrated Catalog	Correlation	Figure	Mmin—Mmax. Initial Magnitude Scale	Note
GCMT	MW	1	138	$M = MW^{GCMT}$		–	4.6–6.4	
ISC	mb	2	979	$M = mb^{ISC} + 0.2$	0.67	15a	3.0–6.3	Gakkel and Knipovich
NEIC, NEIS	mb	2	74	$M = mb^{NEIC} + 0.1$	0.66	15b	3.2–4.8	Gakkel and Knipovich
FCIAR	ML	3	561	$M = ML^{FCIAR} + 0.6$	0.37	19a	2.0–4.3	Gakkel
KOLA	mb	4	32	$M = mb^{KOLA} + 0.2$	0.74	19b	3.1–4.2	Gakkel
MOS	mb	4	1	$M = mb^{MOS}$	0.82	19c	5.3	Gakkel
USCGS	mb	4	2	$M = mb^{USCGS} + 0.2$	0.83	18a	3.8–4.0	Gakkel and Knipovich
BER	Mw	4	23	$M = Mw^{BER} - 0.1$	0.72	16a	3.1–4.1	Gakkel and Knipovich
BER	mb(Pn)	4	30	$M = mb(Pn)^{BER} - 0.1$	0.82	16b	2.6–4.0	Gakkel and Knipovich
BER	ML	5	3	$M = ML^{BER} + 1.2$	0.54	15c	1.9–2.3	Knipovich, unreliable
DNK	ML	5	3	$M = ML^{DNK} + 0.6$	0.79	16c	1.7–2.3	2008–2015.2, Knipovich, unreliable
DNK	ML	5	15	$M = ML^{DNK} + 1.3$	0.57	16d	0.6–2.2	2015.3–2022, Knipovich, unreliable
KOLA	ML	5	24	$M = ML^{KOLA} + 0.5$	0.65	16e	1.3–3.5	Knipovich, unreliable
NAO	ML	4	3	$M = ML^{NAO} + 1.1$	0.53	16f	2.4–2.8	1990–2008, Gakkel and Knipovich
LAO	M	4	5	$M = M^{LAO} + 0.4$	0.79	19d	3.7–4.5	Gakkel
IDC	mb	4	141	$M = mb^{IDC} + 0.2$	0.85	17c	3.2–4.3	Gakkel and Knipovich
EIDC	mb	4	19	$M = mb^{EIDC} + 0.3$	0.76	17d	2.7–3.9	Gakkel and Knipovich
GSR	MPV	4	2	$M = MPV^{GSR}$	0.44	19e	4.4–5.0	Gakkel
ISC	MS	4	1	$M = 0.5MS^{ISC} + 2.88$	0.85	19f	5.3	Gakkel
GSR	MLH	4	4	$M = 0.52MLH^{GSR} + 2.6$	0.75	19g	3.0–3.4	Gakkel
OTT	ML	5	5	$M = ML^{OTT} + 0.1$	0.23	18e	3.2–4.2	Gakkel and Knipovich Poorly determined
GSR	k	5	16	$M = k/2 - 1.2$	0.51	19h	9–11	Gakkel Poorly determined
CSEM	ML	5	2	$M = ML^{CSEM}$		–	2.2–2.6	Not Determined
CGS	M	5	2	$M = M^{CGS}$		–	4.2–4.6	Not Determined
MSCGS	M	5	1	$M = M^{MSCGS}$		–	4.3	Not Determined
PAL	M	5	2	$M = M^{PAL}$		–	4.0–4.8	Not Determined
STU	M	5	1	$M = M^{STU}$		–	4.8	Not Determined
Total			2089					

3.3. Statistics of the Integrated Catalog for Three Sub-Regions

Figure 20 shows the distribution of earthquake epicenters from the created integrated catalog. The catalog contains 17,922 events, 989 events are from Russian catalogs, and the rest are from ISC. In the sub-regions of Svalbard and Knipovich Ridge, the addition of Russian data to ISC is insignificant. However, in the Gakkel Ridge, Russian data accounts for more than a quarter of the events, and more than half since 2012. Detailed statistics are provided in Table 6.

Table 6. Statistics of the integrated catalog.

Time Period, Catalog *	N Total	N from ISC	N from GS RAS, Morozov	Mc	$\frac{N}{M \geq Mc}$	Mmax
1962–2022						
N_Arctic	17,922	16,933 (94.2%)	989 (5.8%)	-		6.7
Svalbard	6921	6617 (95.6%)	304 (4.4%)	-		6.1
Knipovich Ridge	8912	8794 (98.7%)	118 (1.3%)	-		6.7
Gakkel Ridge	2089	1522 (72.9%)	567 (27.1%)	-		6.5
1962–1994						
N_Arctic	703	683 (97.2%)	20 (2.8%)	5.0	181	6.7
Svalbard	94	94 (100%)	0 (0%)	4.5	20	5.6
Knipovich Ridge	329	329 (100%)	0 (0%)	4.7	166	6.7
Gakkel Ridge	280	260 (92.9%)	20 (7.1%)	5.0	102	6.5
1995–2011						
N_Arctic	4377	4261 (97.3%)	116 (2.7%)	4.0	762	6.5
Svalbard	2209	2103 (95.2%)	105 (4.8%)	2.8	696	6.1
Knipovich Ridge	1408	1405 (99.8%)	3 (0.2%)	4.0	275	6.5
Gakkel Ridge	760	752 (98.9%)	8 (1.1%)	4.0	454	6.2
2012–2022						
N_Arctic	12,842	11,989 (95.4%)	853 (6.6%)	4.0	657	6.0
Svalbard	4618	4419 (95.7%)	199 (4.3%)	1.7	2351	5.3
Knipovich Ridge	7175	7060 (98.4%)	115 (1.6%)	2.8	3447	6.0
Gakkel Ridge	1049	510 (48.6%)	539 (51.4%)	4.0*	388	5.9

* Excluding the most eastern segment, where $Mc = 4.5$.

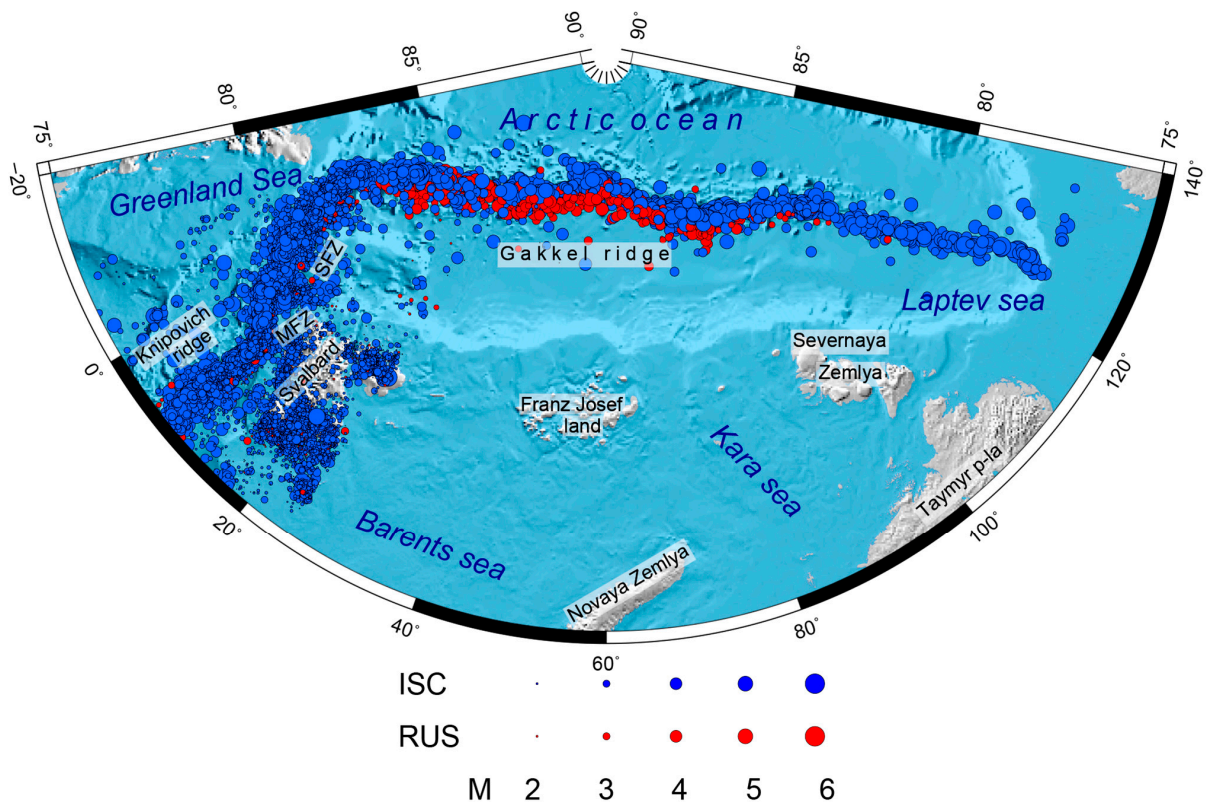


Figure 20. Map of earthquake epicenters $M \geq 2.0$ of the integrated catalog. Blue dots show events from the ISC catalog, and red dots show events from Russian catalogs.

Figures 21–23 show event distributions over time and magnitude, as well as differential magnitude-frequency graphs for various time periods for the sub-regions of Svalbard, Knipovich Ridge, and Gakkel Ridge.

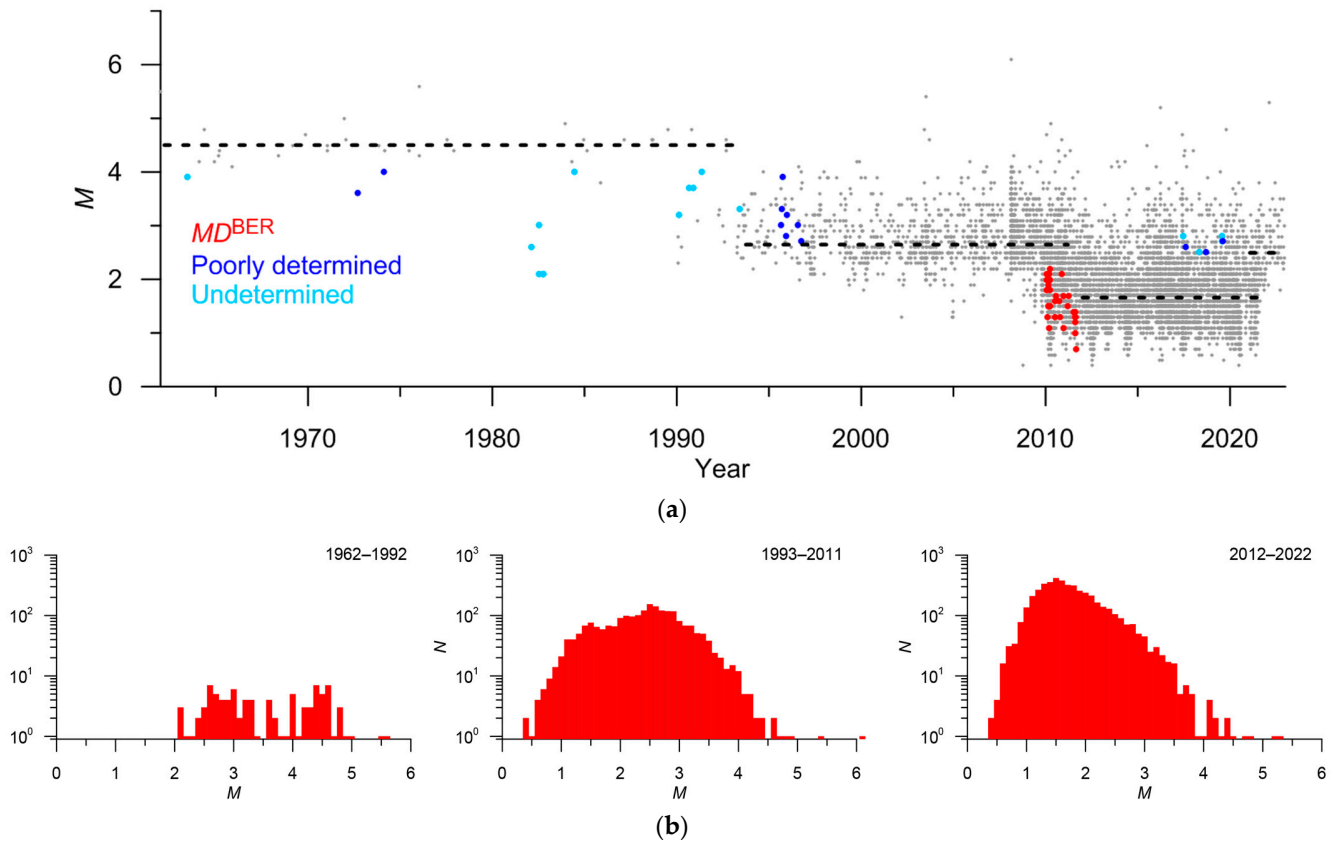


Figure 21. Svalbard. (a) Event distribution over time and unified magnitude; (b) non-cumulative frequency-magnitude distributions in different periods. Colored dots in (a) show events with unreliable magnitudes (Table 3), and the dashed lines show preliminary estimates of completeness magnitude M_c .

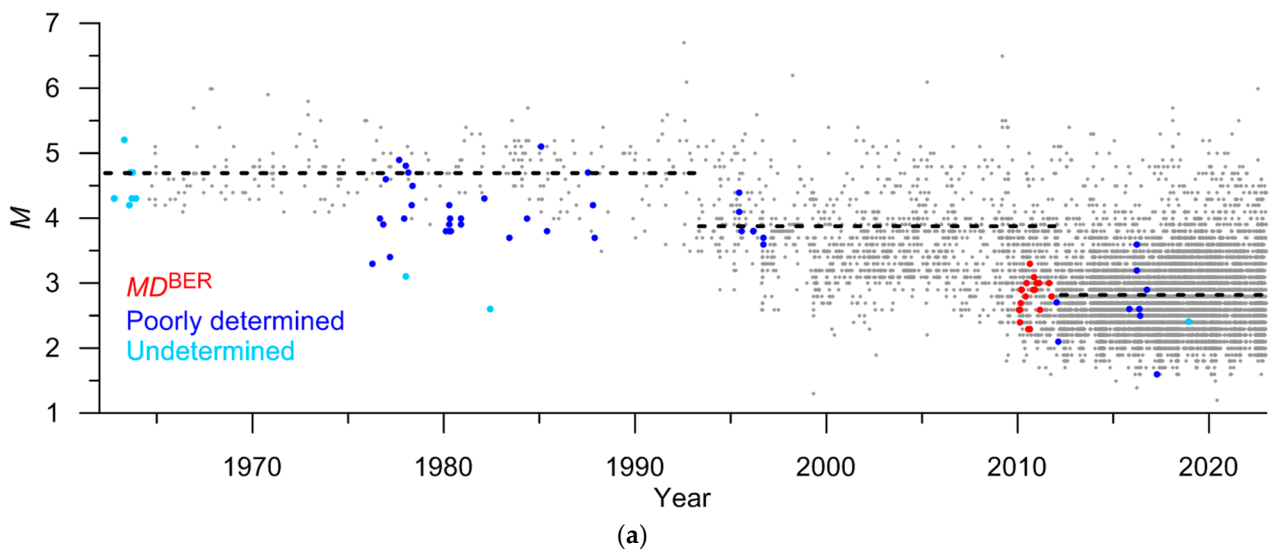


Figure 22. Cont.

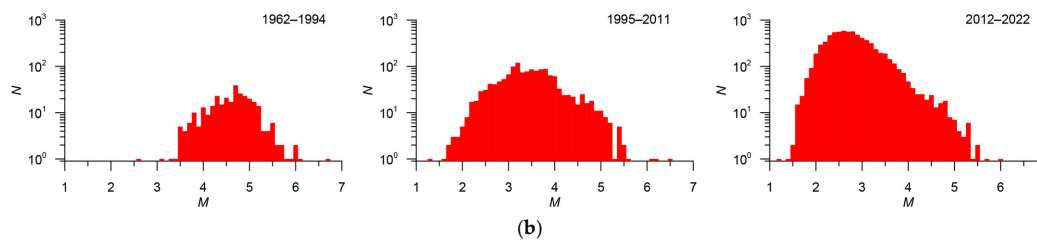


Figure 22. Knipovich Ridge. (a) Event distribution over time and unified magnitude; (b) non-cumulative frequency-magnitude distributions in different periods. Colored dots in (a) show events with unreliable magnitudes (Table 4), and the dashed lines show preliminary estimates of the completeness magnitude M_c .

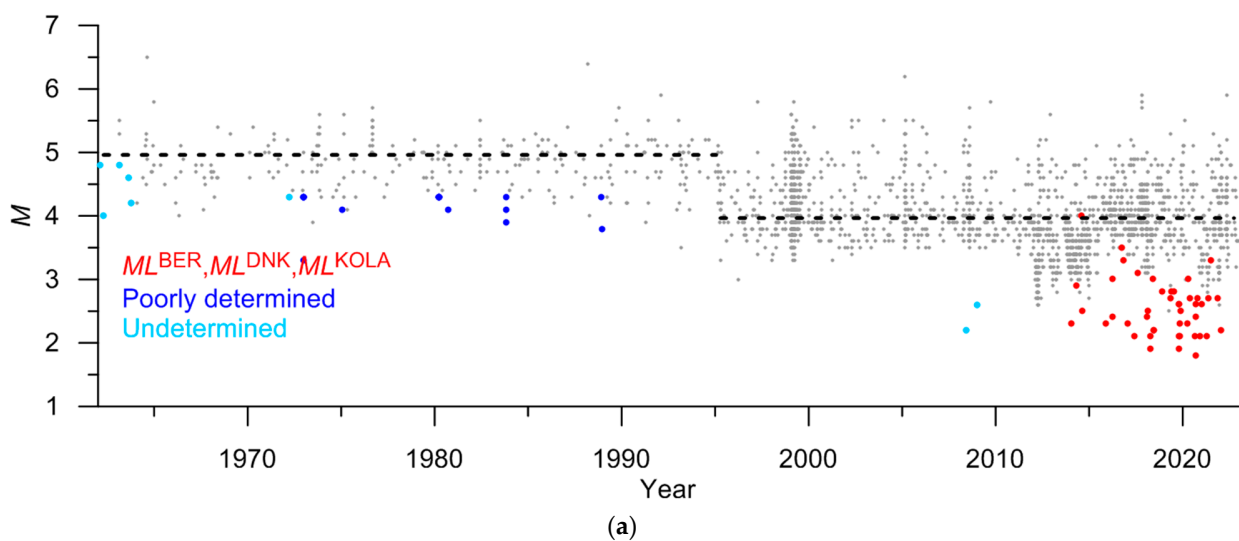


Figure 23. Gakkel Ridge. (a) Event distribution over time and unified magnitude; (b) non-cumulative frequency-magnitude distributions in different periods. Colored dots in (a) show events with unreliable magnitudes (Table 5), and the dashed lines show preliminary estimates of the completeness magnitude M_c .

Figure 24 shows spatial-temporal variations of the magnitude of complete registration M_c , constructed using the multi-scale method. To determine spatial-temporal variations of the magnitude of complete registration, we used the author's multi-scale method [33,34]. It was developed for the analysis of heterogeneous catalogs with significant variations in the registration level. The algorithm was based on adapting the dimension of the studied zone to the range of the event magnitude. We associated ranges of larger magnitudes with increasing areas for data selection. The high resolution of the M_c -value was achieved through the determination of the smallest space-magnitude scale in which the Gutenberg-Richter law is verified. The high accuracy and resolution of the method were confirmed by

testing on real earthquake catalogs and on synthetic data with the prescribed M_c . The data in Table 6 are based on multi-scale analysis, the results of which are presented in Figure 24.

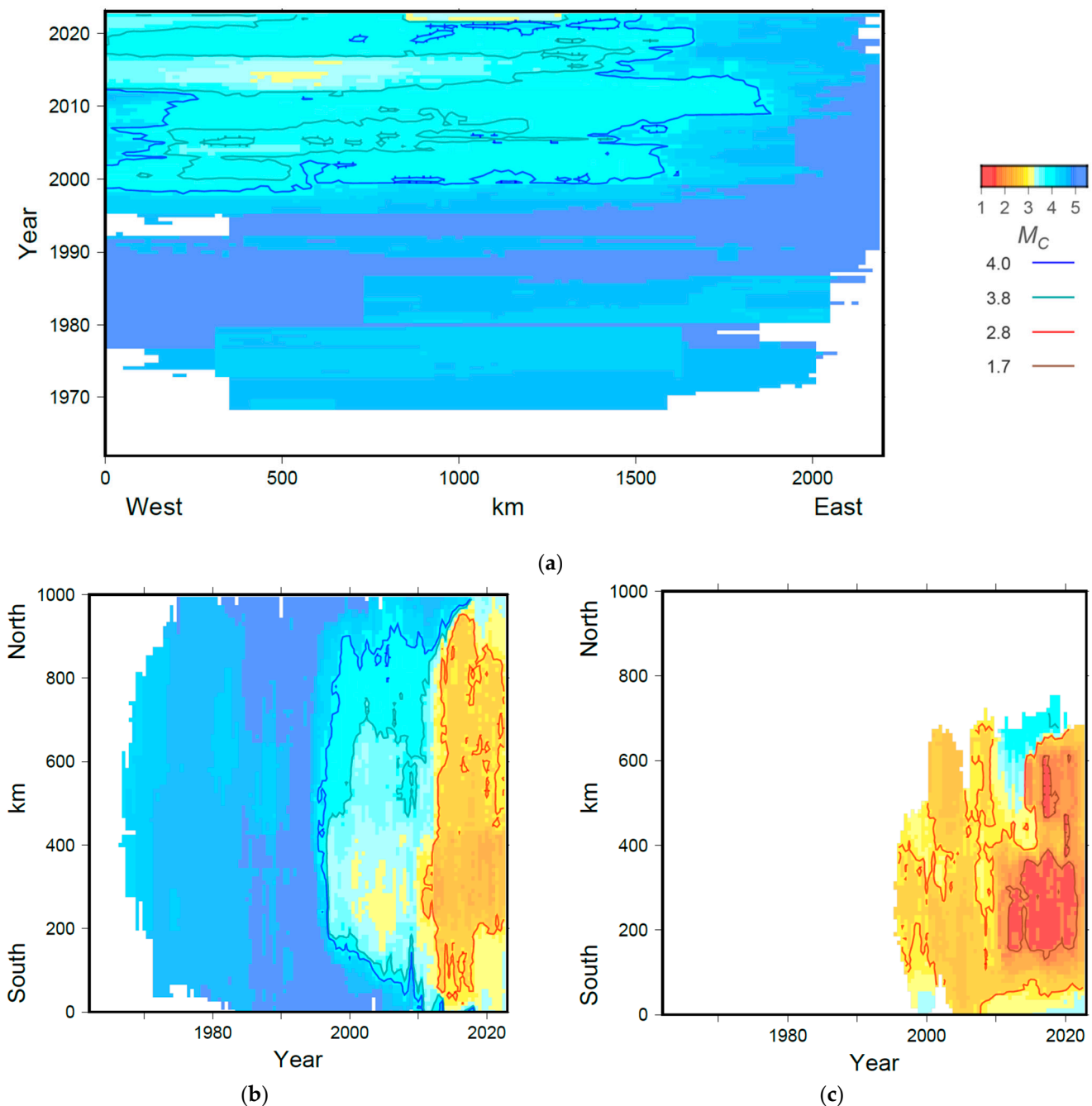


Figure 24. Spatial-temporal variations of the magnitude of complete registration M_c (a) Gakkel Ridge; (b) Knipovich Ridge; (c) Svalbard.

The number of recorded events in the Svalbard Archipelago and the Knipovich Ridge noticeably increased in 2010, but the best level of registration occurred in 2012. In the Gakkel Ridge, the number of weak events significantly increased after 2012 (data from the Arkhangelsk FCIAR network). However, the magnitude of complete registration M_c only decreased in certain spatial-temporal areas, with $M_c = 4.0$ for the region as a whole, except for the easternmost segment where $M_c = 4.5$. The M_c maps are in good agreement with the spatial-temporal distribution of magnitudes (Figure S5, see Supplementary).

4. Conclusions

In this paper, the data from seismic catalogs of various monitoring networks were generalized and integrated using the author's technique [26] based on statistic distribution analysis. The target was to create the most complete and representative earthquake catalog of the Gakkel and Knipovich ridges, as well as the Svalbard Archipelago. The magnitude estimates were unified in the obtained integrated catalog. The earthquake epicenter map of the integrated catalog is shown in Figure 20. The integrated catalog was made available to the public on the website of the World Data Center for Solid Earth Physics, Moscow, at http://www.wdcb.ru/arctic_antarctic/arctic_seism.html (accessed on 1 August 2023).

Based on the conducted study and obtained results, the authors consider it possible to formulate the following conclusions:

1. The earthquake catalogs of the studied region (the Gakkel and Knipovich mid-ocean ridges plus the Svalbard Archipelago) are a mixture of data from a large number of agencies. Moreover, the catalogs significantly vary over time. As a result, heavy tails appear in the DT , DX , and DY distributions. Therefore, determining the threshold value of the metric using the methodology applied in [27,28] leads to an increased probability of missing duplicates. For this reason, in this study, we decided not to use a multivariate normal distribution model. Instead, the actual distribution of the metric for the nearest events from two combined catalogs was used. As a result, the estimated number of errors in the integrated catalog does not exceed 1%;
2. The integrated catalog contains 17,922 events; 16,933 are from the ISC and 989 events are from Russian catalogs. The latter were not presented in the ISC, while the information regarding 578 events from Russian catalogs was used as a part of the ISC data. In the Gakkel Ridge, Russian data accounts for more than a quarter of events, and more than half after 2012. In the sub-regions of Svalbard and Knipovich, the addition of ISC data with Russian catalogs is insignificant. However, an important aspect here is the unification of magnitude;
3. The ratios between local magnitudes M_L with the reference magnitude M_W^{GCMT} and m_b^{ISC} significantly differ in Svalbard and mid-ocean ridges. In Svalbard, the difference between the local and moment magnitudes is about 0.3 (Table 3). In the Knipovich and Gakkel ridges, the estimates of local magnitudes are significantly underestimated compared to the moment magnitude, with a difference exceeding 1.0 (Tables 4 and 5). Figure 25 shows the frequency-magnitude distributions constructed using original magnitudes. In Svalbard, noticeable discontinuities in the distribution are observed (Figure 25a). This can significantly affect the estimates of the b-value (the slope of the magnitude-frequency plot), which is an important parameter in seismic hazard assessment. The distribution in the Knipovich Ridge (Figure 25b) has a bimodal character, which contradicts the Gutenberg-Richter law. This is an independent confirmation of the inconsistency of magnitude estimates M_L and M_W^{GCMT} , m_b^{ISC} . In the Gakkel Ridge (Figure 25c), the distribution weakly follows the Gutenberg-Richter law. After the proposed magnitude conversion, the magnitude-frequency plots acquired a common form (Figures 21b, 22b and 23b);
4. When creating the unified magnitude scale, ratios were used with three types of magnitude, M_W^{GCMT} , m_b^{ISC} , and M_L^{BER} , which are well represented in the studied region. The shift-type ratios turned out to be very similar for most magnitudes of different types determined by various agencies. This approach allows for a significant expansion of the interval for converting magnitudes to proxy- M_W , increases statistics, and thus increases the reliability of the conversion. The M_W^{GCMT} magnitude is only determined for strong earthquakes with $M > 5.0$. The use of correlations with m_b^{ISC} and M_L^{BER} allows for an extension of the interval to M of the order of 1. Strictly mathematically, this is not proof of the linearity of ratios between different magnitudes, but it is a weighty argument in favor of such an assumption;
5. The level of registration significantly varies over time and differs in sub-regions. The best registration level is on Svalbard ($M_c = 1.7$ after 2012), where there are many

- seismic stations of the BER, NORSAR, and KOLA networks. A good registration level is apparent in the Knipovich Ridge ($M_c = 2.8$ after 2012), which is provided by Norwegian and Russian stations on Svalbard and Danish DNK stations in Greenland. The worst registration level is in the Gakkel Ridge ($M_c = 4.0$), which is not surprising. The nearest seismic stations of FCIAR are located on the archipelagos of Severnaya Zemlya and Franz Josef Land, approximately 600 km from the seismic zone. The distance from Svalbard stations to the Gakkel Ridge is approximately the same;
- The integrated earthquake catalog created and reported in this paper is intended for a wide range of researchers involved in both the study of the seismic regime of the Arctic and, in general, seismic hazard assessment [35–46]. Presented here, the integrated earthquake catalog, along with the author's Arctic catalogs [27,28], provides an important contribution to the development of an Arctic Big Data system. Its creation is one of the important requirements for starting a full-scale system analysis of geophysical dynamics in the Arctic;
 - Figure S6 (see Supplementary) presents all three created integrated earthquake catalogs for the Arctic zone of the Russian Federation. The integrated catalog of Arctic regions I, II, and III contains 45,793 events. In the Svalbard region, 12 duplicates were identified and removed. We believe that the magnitude scale is homogeneous, because all magnitudes were converted to *proxi-M_w*. The catalog is available to the public at: http://www.wdcb.ru/arctic_antarctic/arctic_seism.html (accessed on 1 August 2023).

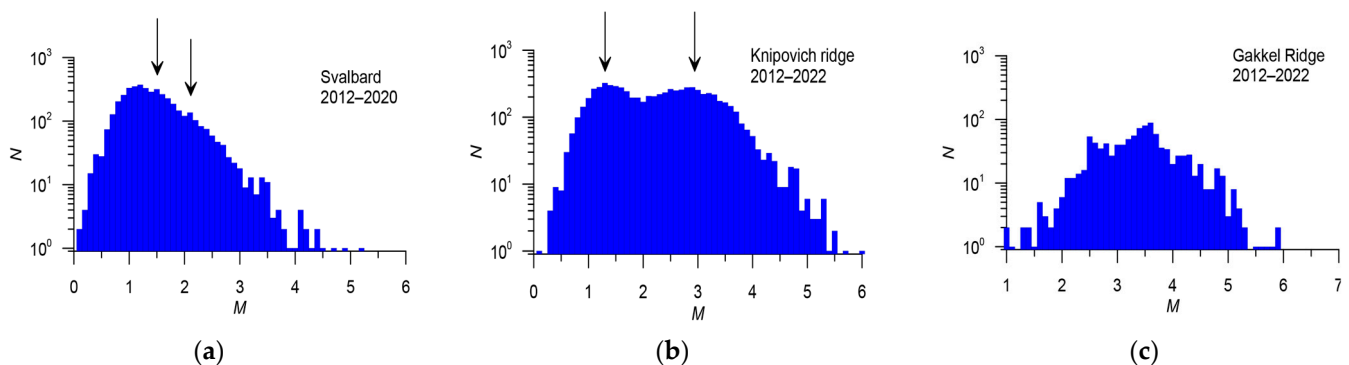


Figure 25. Non-cumulative frequency-magnitude distributions constructed using original magnitudes. (a) Svalbard, arrows mark discontinuities in distribution. (b) Knipovich Ridge, arrows mark two modes of distribution. (c) Gakkel Ridge, distribution weakly follows the Gutenberg-Richter law.

Supplementary Materials: The following supporting information can be downloaded at: <https://www.mdpi.com/article/10.3390/app132212422/s1>, Figure S1: Schematic coverage map for catalogs I (Eastern Sector), II (Western Sector) and III (75° N, 10° W; 88° N, 10° W; 88° N, 140° E; 77° N, 140° E; 77° N, 100° E; 84° N, 100° E; 84° N, 25° E; 75° N, 25° E). It includes the Svalbard Archipelago and adjacent areas (75° N–84° N, 10° E–25° E), the Knipovich Ridge, Molloy and Spitsbergen fracture zones (75° N–83° N, 10° W–10° E), and the Gakkel Ridge (the rest of the studied area); Table S1: Statistics of the ISC catalog; Figure S2: Distribution of focal depth for events with $M \leq 2.2$ in Svalbard; Figure S3: Distribution of the metric for events within the source earthquake catalogs (Table 1). The catalog name is indicated on the histogram; Figure S4: Modified Figure 9. Magenta line in (b) shows the probability of missing a duplicate in the model of multivariate normal distribution, green line shows the total probability of the first and the second kind errors. Dashed green line in (a) and (b) shows threshold value of $R_o = 7$, minimizing total error. (c) Green contour line of the metric (1) $R_o = 7$ shows obvious missing of duplicates; Figure S5: Distribution of earthquakes in space and time. (a) Gakkel ridge; (b) Knipovich ridge; (c) Svalbard.; Figure S6: Map of earthquake epicenters of three created integrated catalogs: I (Eastern Sector), II (Western Sector) and III (Gakkel Ridge, Knipovich Ridge and Svalbard Archipelago).

Author Contributions: Conceptualization, I.A.V., A.D.G. and P.N.S.; Data curation, P.N.S., B.A.D., B.V.D., N.A.S., E.O.K. and Y.V.B.; Formal analysis, I.A.V.; Investigation, P.N.S., B.A.D., B.V.D. and

E.O.K.; Methodology, I.A.V.; Resources, B.A.D., B.V.D., N.A.S. and E.O.K.; Software, I.A.V.; Validation, I.A.V., A.D.G., P.N.S., B.A.D. and B.V.D.; Visualization, I.A.V., B.V.D. and Y.V.B.; Writing—original draft, I.A.V., A.D.G., P.N.S., B.A.D., B.V.D., N.A.S., E.O.K. and Y.V.B.; Writing—review and editing, I.A.V., A.D.G., P.N.S., B.A.D., B.V.D., N.A.S., E.O.K. and Y.V.B. All authors have read and agreed to the published version of the manuscript.

Funding: The reported study was funded by the Russian Science Foundation, project number 21-77-30010 «System analysis of geophysical process dynamics in the Russian Arctic and their impact on the development and operation of the railway infrastructure».

Institutional Review Board Statement: Not applicable.

Informed Consent Statement: Not applicable.

Data Availability Statement: Data are contained within the article and Supplementary Materials.

Acknowledgments: This work employed data provided by the Shared Research Facility «Analytical Geomagnetic Data Center» of the Geophysical Center of RAS (<http://ckp.gcras.ru/> accessed on 1 August 2023). The data used in the work were obtained with large-scale research facilities «Seismic infrasound array for monitoring Arctic cryolithozone and continuous seismic monitoring of the Russian Federation, neighboring territories and the world». This work employed data provided by the International Seismological Centre (2023), Seismological Dataset Repository, <https://doi.org/10.31905/6TJZECEY> (accessed on 1 August 2023).

Conflicts of Interest: The authors declare no conflict of interest.

Abbreviations

The following abbreviations for seismological agencies are used in this manuscript:

BCIS	Bureau Central International de Sismologie, France
BER	University of Bergen, Norway
CSEM	Centre Sismologique Euro-Méditerranéen (CSEM/EMSC), France
DNK	Geological Survey of Denmark and Greenland, Denmark
EIDC	Experimental (GSETT3) International Data Center, USA
FCIAR	Federal Center for Integrated Arctic Research, Russia
GFZ	Helmholtz Centre Potsdam GFZ German Research Centre For Geosciences, Germany
HEL	Institute of Seismology, University of Helsinki, Finland
HFS	Hagfors Observatory, Sweden
IDC	International Data Centre, CTBTO, Austria
IEPN	Institute of Environmental Problems of the North, Russian Academy of Sciences, Russia
INMG	Instituto Português do Mar e da Atmosfera, I.P., Portugal
ISC	International Seismological Centre, United Kingdom
ISS	International Seismological Summary, United Kingdom
MOS	Geophysical Survey of Russian Academy of Sciences (GS RAS), Russia
KOLA	Kola Regional Seismic Centre, GS RAS, Russia
MSUGS	Michigan State University, Department of Geological Sciences, USA
NAO	Stiftelsen NORSAR, Norway
NEIC	National Earthquake Information Center, USA
OTT	Canadian Hazards Information Service, Natural Resources Canada
SYKES	Sykes Catalogue of earthquakes 1950 onwards
WAR	Institute of Geophysics, Polish Academy of Sciences, Poland
ZEMSU	USSR

References

1. Thiede, J.; The Shipboard Scientific Party. Polarstern Arctis XVII/2 Cruise Report: AMORE 2001 (Arctic Mid-Ocean Ridge Expedition). *Alfred Wegener Inst.* **2002**, *421*, 297.
2. Schlindwein, V.; Muller, C.C.; Jokat, W. Microseismicity of the Ultraslow-Spreading Gakkel Ridge, Arctic Ocean: A Pilot Study. *Geophys. J. Int.* **2007**, *169*, 100–112. [[CrossRef](#)]
3. Muller, C.; Jokat, W. Seismic evidence for volcanic activity discovered in Central Arctic. *Eos Trans. AGU* **2000**, *81*, 265–269. [[CrossRef](#)]
4. Tolstoy, M.; Bohnenstiehl, D.R.; Edwards, M.H.; Kurras, G.J. Seismic character of volcanic activity at the ultraslow-spreading Gakkel Ridge. *Geology* **2001**, *29*, 1139–1142. [[CrossRef](#)]
5. Cochran, J.R.; Kurras, G.J.; Edwards, M.H.; Coakley, B.J. The Gakkel Ridge: Bathymetry, gravity anomalies and crustal accretion at extremely slow spreading rates. *J. Geophys. Res. Solid Earth* **2003**, *108*, 2116–2137. [[CrossRef](#)]
6. Cochran, J.R. Seamount volcanism along the Gakkel ridge, Arctic Ocean. *Geophys. J. Int.* **2008**, *174*, 1153–1173. [[CrossRef](#)]
7. Michael, P.J.; Langmuir, C.H.; Dick, H.J.B.; Snow, J.E.; Goldsteink, S.L.; Graham, D.W.; Lehnert, K.; Kurras, G.; Jokat, W.; Muhe, R.; et al. Magmatic and amagmatic seafloor generation at the ultraslow-spreading Gakkel ridge, Arctic Ocean. *Nature* **2003**, *423*, 956–961. [[CrossRef](#)] [[PubMed](#)]
8. Dick, H.; Lin, J.; Schouten, H. An ultraslow-spreading class of ocean ridge. *Nature* **2003**, *426*, 405–412. [[CrossRef](#)] [[PubMed](#)]
9. Zarayskaya, Y.A. Segmentation and seismicity of the ultraslow Knipovich and Gakkel mid-ocean ridges. *Geotectonics* **2017**, *51*, 163–175. [[CrossRef](#)]
10. Dubinin, E.P.; Kokhan, A.V.; Sushchevskaya, N.M. Tectonics and magmatism of ultraslow spreading ridges. *Geotectonics* **2013**, *47*, 131–155. [[CrossRef](#)]
11. Jokat, W.; Schmidt-Aursch, M. Geophysical characteristics of the ultraslow spreading Gakkel Ridge, Arctic Ocean. *Geophys. J. Intern.* **2007**, *168*, 983–998. [[CrossRef](#)]
12. Kokhan, A.V.; Dubinin, E.P.; Grokholsky, A.L. Geodynamical peculiarities of structure-forming in Arctic and Polar Atlantic spreading ridges. *Bull. Kamchatka Reg. Assoc.* **2012**, *19*, 59–77. (In Russian)
13. Koulakov, I.; Schlindwein, V.; Liu, M.; Gerya, T.; Jakovlev, A.; Ivanov, A. Low-degree mantle melting controls the deep seismicity and explosive volcanism of the Gakkel Ridge. *Nat. Commun.* **2022**, *13*, 3122. [[CrossRef](#)] [[PubMed](#)]
14. Assinovskaya, B.A.; Panas, N.M.; Ovsov, M.K.; Antonovskaya, G.N. Preliminary seismic hazard assessment of the Arctic Gakkel ridge and surrounding. *Russ. J. Seismol.* **2019**, *1*, 35–45. [[CrossRef](#)]
15. Di Giacomo, D.; Engdahl, E.R.; Storchak, D.A. The ISC–GEM Earthquake Catalogue (1904–2014): Status after the Extension Project. *Earth Syst. Sci. Data* **2018**, *10*, 1877–1899. [[CrossRef](#)]
16. Ekström, G.; Nettles, M.; Dziewonski, A.M. The global CMT project 2004–2010: Centroid-moment tensors for 13,017 earthquakes. *Phys. Earth Planet. Inter.* **2012**, *200–201*, 1–9. [[CrossRef](#)]
17. Köhler, A.; Gajek, W.; Malinowski, M.; Schweitzer, J.; Majdanski, M.; Geissler, W.H.; Chamarczuk, M.; Wuestefeld, A. Seismological monitoring of Svalbard’s cryosphere: Current status and knowledge gaps. In SESS report 2019—The State of Environmental Science in Svalbard—An annual report. *Svalbard Integr. Arct. Earth Obs. Syst.* **2020**, *1*, 136–159. [[CrossRef](#)]
18. Asming, V.E.; Fedorov, A.V.; Alenicheva, A.O.; Jevtjugina, Z.A. Usage of the NSDL Location System for the Detailed Study of the Spitsbergen Archipelago Seismicity. *Her. Kola Sci. RAS* **2018**, *3*, 120–131. (In Russian) [[CrossRef](#)]
19. Baranov, S.V. The aftershock process of the February 21, 2008 Storfjorden strait, Spitsbergen, earthquake. *J. Volcanol. Seismol.* **2013**, *7*, 230–242. [[CrossRef](#)]
20. Sokolov, S.Y. Tectonic evolution of the Knipovich Ridge based on the anomalous magnetic field. *Dokl. Earth Sci.* **2011**, *437*, 343–348. [[CrossRef](#)]
21. Crane, K.; Doss, H.; Vogt, P.; Sundvor, E.; Cherkashov, G.; Poroshina, I.; Joseph, D. The role of the Spitsbergen shear zone in determining morphology, segmentation and evolution of the Knipovich Ridge. *Mar. Geophys. Res.* **2001**, *22*, 153–205. [[CrossRef](#)]
22. Morozov, A.N.; Vaganova, N.V.; Starkov, I.V.; Mikhaylova, Y.A. Modern Low-Magnitude Earthquake Swarms of the Gakkel Mid-Oceanic Ridge, Arctic Ocean. *Russ. J. Earth. Sci.* **2023**, *23*, ES3007. [[CrossRef](#)]
23. Antonovskaya, G.; Morozov, A.; Vaganova, N.; Konechnaya, Y. Seismic monitoring of the European Arctic and Adjoining Regions. In *The Arctic: Current Issues and Challenges*; Pokrovsky, O.S., Kirpotin, S.N., Malov, A.I., Eds.; Nova Science Publishers, Inc.: New York, NY, USA, 2020; pp. 303–368.
24. Engen, Ø.; Eldholm, O.; Bungum, H. The Arctic plate boundary. *J. Geophys. Res.* **2003**, *108*, 2075. [[CrossRef](#)]
25. Shebalin, P.N.; Baranov, S.V.; Dzeboev, B.A. The Law of the Repeatability of the Number of Aftershocks. *Dokl. Earth Sci.* **2018**, *481*, 963–966. [[CrossRef](#)]
26. Vorobieva, I.; Gvishiani, A.; Dzeboev, B.; Dzeranov, B.; Barykina, Y.; Antipova, A. Nearest Neighbor Method for Discriminating Aftershocks and Duplicates When Merging Earthquake Catalogs. *Front. Earth Sci.* **2022**, *10*, 820277. [[CrossRef](#)]
27. Gvishiani, A.D.; Vorobieva, I.A.; Shebalin, P.N.; Dzeboev, B.A.; Dzeranov, B.V.; Skorkina, A.A. Integrated Earthquake Catalog of the Eastern Sector of the Russian Arctic. *Appl. Sci.* **2022**, *12*, 5010. [[CrossRef](#)]
28. Vorobieva, I.A.; Gvishiani, A.D.; Shebalin, P.N.; Dzeboev, B.A.; Dzeranov, B.V.; Skorkina, A.A.; Sergeeva, N.A.; Fomenko, N.A. Integrated Earthquake Catalog II: The Western Sector of the Russian Arctic. *Appl. Sci.* **2023**, *13*, 7084. [[CrossRef](#)]
29. Morozov, A.N.; Vaganova, N.V.; Asming, V.E.; Peretokin, S.A.; Aleshin, I.M. Seismicity of the Western Sector of the Russian Arctic. *Phys. Solid Earth* **2023**, *59*, 209–241. [[CrossRef](#)]

30. Vinogradov, Y.A.; Asming, V.E.; Baranov, S.V.; Fedorov, A.V.; Vinogradov, A.N. Seismic and infrasonic monitoring of glacier destruction: A pilot experiment on Svalbard. *Seism. Instr.* **2015**, *51*, 1–7. [[CrossRef](#)]
31. Bogorodskiy, P.V.; Demidov, N.E.; Filchuk, K.V.; Marchenko, A.V.; Morozov, E.G.; Nikulina, A.L.; Pnyushkov, A.V.; Ryzhov, I.V. Growth of land fast ice and its thermal interaction with bottom sediments in the Braganzavägen Gulf (West Spitsbergen). *Russ. J. Earth Sci.* **2020**, *20*, ES6005. [[CrossRef](#)]
32. Di Giacomo, D.; Bondár, I.; Storchak, D.A.; Engdahl, E.R.; Bormann, P.; Harris, J. ISC-GEM: Global Instrumental Earthquake Catalogue (1900–2009), III. Re-computed MS and mb, proxy MW, final magnitude composition and completeness assessment. *Phys. Earth Planet. Inter.* **2015**, *239*, 33–47. [[CrossRef](#)]
33. Vorobieva, I.; Shebalin, P.; Narteau, C.; Beauducel, F.; Necessian, A.; Clouard, V.; Bouin, M.-P. Multiscale mapping of completeness magnitude of earthquake catalogs. *Bull. Seism. Soc. Am.* **2013**, *103*, 2188–2202. [[CrossRef](#)]
34. Vorobieva, I.; Shebalin, P.; Narteau, C. Break of slope in earthquake size distribution and creep rate along the San Andreas Fault system. *Geophys. Res. Lett.* **2016**, *43*, 6869–6875. [[CrossRef](#)]
35. Agayan, S.M.; Tatarinov, V.N.; Gvishiani, A.D.; Bogoutdinov, S.R.; Belov, I.O. FDPS algorithm in stability assessment of the Earth's crust structural tectonic blocks. *Russ. J. Earth Sci.* **2020**, *20*, ES6014. [[CrossRef](#)]
36. Dzeboev, B.A.; Gvishiani, A.D.; Agayan, S.M.; Belov, I.O.; Karapetyan, J.K.; Dzeranov, B.V.; Barykina, Y.V. System-Analytical Method of Earthquake-Prone Areas Recognition. *Appl. Sci.* **2021**, *11*, 7972. [[CrossRef](#)]
37. Dzeboev, B.A.; Karapetyan, J.K.; Aronov, G.A.; Dzeranov, B.V.; Kudin, D.V.; Karapetyan, R.K.; Vavilin, E.V. FCAZ-recognition based on declustered earthquake catalogs. *Russ. J. Earth Sci.* **2020**, *20*, ES6010. [[CrossRef](#)]
38. Gorshkov, A.I.; Soloviev, A.A. Recognition of earthquake-prone areas in the Altai-Sayan-Baikal region based on the morphostructural zoning. *Russ. J. Earth Sci.* **2021**, *21*, ES1005. [[CrossRef](#)]
39. Gvishiani, A.D.; Soloviev, A.A.; Dzeboev, B.A. Problem of Recognition of Strong-Earthquake-Prone Areas: A State-of-the-Art Review. *Izv. Phys. Solid Earth* **2020**, *56*, 1–23. [[CrossRef](#)]
40. Kossobokov, V.G.; Soloviev, A.A. Pattern recognition in problems of seismic hazard assessment. *Chebyshevskii Sb.* **2018**, *19*, 55–90. (In Russian) [[CrossRef](#)]
41. Peresan, A.; Gorshkov, A.; Soloviev, A.; Panza, G.F. The contribution of pattern recognition of seismic and morphostructural data to seismic hazard assessment. *Boll. Di Geofis. Teor. Ed Appl.* **2015**, *56*, 295–328. [[CrossRef](#)]
42. Gorshkov, A.; Kossobokov, V.; Soloviev, A. Recognition of earthquake-prone areas. In *Nonlinear Dynamics of the Lithosphere and Earthquake Prediction*; Keilis-Borok, V., Soloviev, A., Eds.; Springer: Heidelberg, Germany, 2003; pp. 239–310. [[CrossRef](#)]
43. Peresan, A.; Zuccolo, E.; Vaccari, F.; Gorshkov, A.; Panza, G.F. Neo-deterministic seismic hazard and pattern recognition techniques: Time-dependent scenarios for North-Eastern Italy. *Pure Appl. Geophys.* **2011**, *168*, 583–607. [[CrossRef](#)]
44. Gorshkov, A.I.; Panza, G.F.; Soloviev, A.A.; Aoudia, A. Morphostructural zonation and preliminary recognition of seismogenic nodes around the Adria margin in peninsular Italy and Sicily. *J. Seismol. Earthq. Eng.* **2002**, *4*, 1–24.
45. Gorshkov, A.; Novikova, O.; Parvez, I.A. Recognition of earthquake-prone areas in the Himalaya: Validity of the results. *Int. J. Geophys.* **2012**, *2012*, 419143. [[CrossRef](#)]
46. Gorshkov, A.; Novikova, O. Estimating the validity of the recognition results of earthquake-prone areas using the ArcMap. *Acta Geophys.* **2018**, *66*, 843–853. [[CrossRef](#)]

Disclaimer/Publisher's Note: The statements, opinions and data contained in all publications are solely those of the individual author(s) and contributor(s) and not of MDPI and/or the editor(s). MDPI and/or the editor(s) disclaim responsibility for any injury to people or property resulting from any ideas, methods, instructions or products referred to in the content.